

# We are IntechOpen, the world's leading publisher of Open Access books Built by scientists, for scientists

6,900

Open access books available

185,000

International authors and editors

200M

Downloads

Our authors are among the

154

Countries delivered to

TOP 1%

most cited scientists

12.2%

Contributors from top 500 universities



WEB OF SCIENCE™

Selection of our books indexed in the Book Citation Index  
in Web of Science™ Core Collection (BKCI)

Interested in publishing with us?  
Contact [book.department@intechopen.com](mailto:book.department@intechopen.com)

Numbers displayed above are based on latest data collected.  
For more information visit [www.intechopen.com](http://www.intechopen.com)



# Monte Carlo Simulation of Room Temperature Ballistic Nanodevices

Ignacio Íñiguez-de-la-Torre, Tomás González,  
Helena Rodilla, Beatriz G. Vasallo and Javier Mateos  
*Universidad de Salamanca, Departamento de Física Aplicada  
Spain*

## 1. Introduction

The widespread use of digital broadband communications generates a huge amount of data to be processed and transmitted in the fastest possible way. To this end, the development of new electronic devices, digital and analog, able to perform data processing at ultra-high bit rates and to transmit at high frequency is necessary. In the last decade, higher frequencies have been obtained when downscaling traditional HEMTs with high In content InGaAs channels providing cut-off frequencies above 1 THz [Lai et al., 2007]. However, the reduction of the gate length below 30 nm does not provide an improvement of the device performance, obstructed by the influence of the device parasitics and the appearance of important short channel effects. A wide variety of alternatives have been proposed in order to continue improving high frequency performance of electronic devices. One promising solution is the use of new nanometer-scale ballistic transport devices based on high mobility III-V compound heterostructures. The use of advanced electron-beam lithography tools and conventional epitaxial growth techniques for III-V materials also allows the fabrication of a two-dimensional electron gas (2DEG) structures with sizes smaller than the electron mean free path ( $l_m$ ). In these new devices, by smartly custom-made geometries, electrons move like billiard balls, guided by strategically placed shapes, edges and internal deflectors rather than applied voltages [Song, 2004]. The nano-scale dimension of these devices facilitates electron transport with almost no scattering event and is referred as ballistic transport or at least quasi-ballistic and can be observed even at room temperature (RT). This involves not only the presence of velocity overshoot, which can improve the cut-off frequency of classical FET devices, but also gives birth to some new effects and applications with specially designed structures. The great performance of these nanodevices obtained with InGaAs in the channel can be even better, providing higher cut-off frequencies, by using narrow bandgap semiconductors like InAs and InSb [Suyatin et al., 2008].

Now, we introduce some examples of this *family* of nanostructures. In particular, Three-Branch Junctions [Fig. 1(a)] (TBJs, T- and Y-shaped) [Palm & Thylen, 1992; Palm & Thylen, 1996; Worschech et al., 2001a; Shorubalko et al., 2001; Xu, 2001] exhibit a parabolic negative potential at the central branch when biasing in push-pull fashion the left and right branches (in contrast with the zero central potential expected for diffusive structures) [Mateos et al., 2003a; Mateos et al., 2004; Rashmi et al., 2005; Bednarz et al., 2006; Íñiguez-de-la-Torre et al., 2007]. Similar effects take place in ballistic rectifying devices achieved by inserting an

obstacle (antidot) of triangular or diamond shape in the centre of a ballistic cross junction [Song et al., 1998; Song et al., 2001, Vasallo et al., 2004; González et al., 2004]. This type of geometry has also recently been improved by attaching two strategically placed in-plane gates for the fabrication of the so called Ballistic Deflection Transistors (BDT) [Wesström, 1999; Hieke & Ulfward 2000; Diduck et al., 2009; Kaushal et al., 2010]. Ultrafast rectifying nano-diodes, named Self-Switching Diodes (SSDs) [Fig. 1(b)], made with a single-step lithographic process that breaks the symmetry of a narrow channel, have also been successfully fabricated [Song et al., 2003] and simulated [Mateos et al., 2005]. As a consequence of their nonlinear properties, all of these devices have demonstrated manifold functionalities as: wave rectification, frequency doubling and Boolean logic operation, and can work at very high frequencies. Perhaps, most important from the point of view of circuit applications, is that they work at RT. For example, SSDs have been shown to operate as detectors even reaching the THz range [Balocco et al., 2005; Balocco et al., 2008]. However, due to its large impedance and the influence of contact parasitic capacitances, mixing and frequency doubling in TBJs at RT have only been measured below the GHz range [Lewén et al., 2002], and the rectifying effect up to 20 GHz [Worschech et al., 2001b; Worschech et al., 2002] (up to 40 GHz in a double Y branch configuration [Bednarz et al., 2005]). This new family of ballistic nanodevices are ideal candidates to constitute the base for the fabrication of analog/digital circuits to process and transmit data at THz frequencies and at RT. Moreover, these material systems ensure a full compatibility with HEMT technology, which can be used for the post-processing of the output signals.

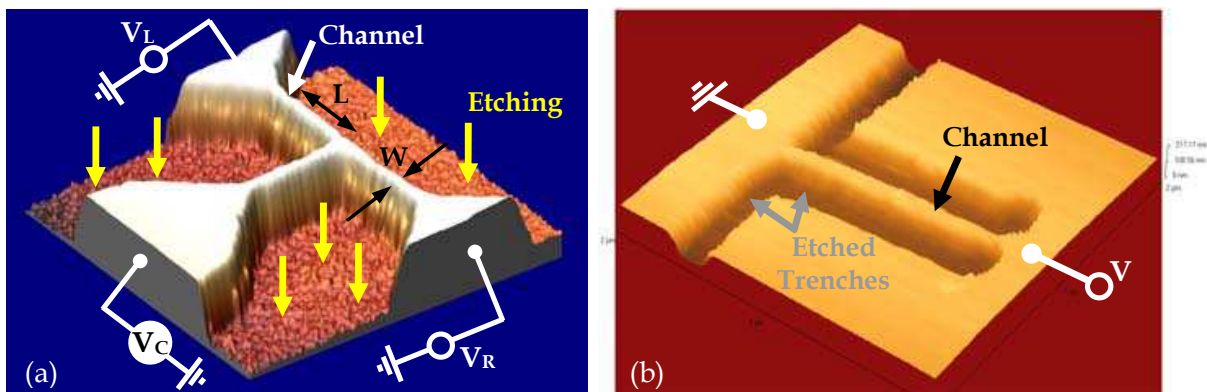


Fig. 1. (a) Atomic force micrographs of a typical (a) TBJ and (b) SSD.

When such new and promising strategies are explored, the test-and-error approach is not efficient at all. At this point, the development of theoretical models and numerical simulations can be of great help. Under these ballistic or quasiballistic conditions, the classic drift-diffusion or hydrodynamic models, traditionally used for device simulation and design, are not appropriate any more. Even if some theoretical descriptions of the operation of ballistic devices have been proposed, always starting from a coherent transport model based on the Landauer-Büttiker formalism [Landauer, 1957; Büttiker, 1986; Song, 1999], the most adequate numerical technique is the Monte Carlo (MC) method [Jacoboni & Lugli, 1989], especially for RT operation. In particular, the MC technique incorporates in a natural way all the scattering mechanisms, so it is able to correctly account for ballistic or quasi-ballistic transport and provide not only static results but also the dynamic and noise behaviour of the devices. Monte Carlo simulations have been proven as an exceptional useful tool for the optimization of the ballistic nanodevices like cross junctions [González et al., 2004], BDTs [Kaushal et al., 2010],

or the TBJ-based multiplexor/de-multiplexor [Mateos et al., 2003a]. In this chapter, by means of our Monte Carlo simulators, we will focus our attention on designing and optimizing TBJs and SSDs to operate at sub-millimetre frequencies and RT. Taking as a base the knowledge of the internal microscopic processes, we will exploit the ballistic effects when the size of the structures is reduced below the electron mean free path. Monte Carlo simulations are able to identify and explain the physical origin of the nonlinear effects in this *family* of nanostructures: (i) electrostatic effects typically associated with the presence of surface charges and (ii) asymmetrical charge distributions related to ballistic transport. Due to the nanometer length associated with ballistic transport, intrinsic operation up to THz frequencies is expected [Mateos et al., 2003b]. However, to really exploit the estimated intrinsic high speed these technologies require more efforts directed towards a proper design of accesses. Reduce cross-talk (extrinsic) capacitances and extrinsic resistances or fabricating devices in parallel in order to reduce the intrinsic impedance without increasing the capacitance will be one of the main challenges. In addition, as the size of electronic devices is reduced, the surface/volume ratio considerably increases and, in strong contrast to conventional devices, when sizes reach the nanometer scale, surface effects can get to have a remarkable importance on electron transport, even becoming decisive in the device behaviour. Also, at this nanometer scale, modelling of the contacts has proven to be crucial. The specific models implemented in the Monte Carlo simulators to deal with these devices as dynamic surface charge models [Íñiguez-de-la-Torre et al., 2007], injection statistics [González et al., 1999], etc, will be explained in this chapter.

The outline of this chapter is as follows. Firstly, in Section II the physical model used for the MC simulation of the ballistic structures is explained. We put special emphasis on the modelling of the surface charge, providing the details of the algorithm. Section III is dedicated to examine the dependence of the well-known parabolic behaviour of the output voltage of TBJs on the size of their branches. Results concerning to the frequency response are also discussed. In Section IV we successfully apply our model to explain the physics underlying the SSD rectifying behaviour and to analyze the AC response and noise spectra dependence on the topology of the devices. A systematic study of channel length and width of the trenches is shown to provide design indications to improve their performance. Finally the main conclusions of the present work are summarized.

## 2. Monte Carlo method. Methodology

In this chapter, the ballistic nanodevices have been studied by analyzing the results obtained using a semi-classical *ensemble* MC simulator self-consistently coupled with a 2D Poisson solver (PS) [Jacoboni & Lugli, 1989]. The transport model locally takes into account the effect of degeneracy and electron heating by using the rejection technique and the self-consistent calculation of the local electronic temperature and Fermi level [Mateos et al., 2000a]. The surface charges appearing at the boundaries of the semiconductors in contact with dielectrics are also considered in the model [Mateos et al., 1999]. The validity of this simulation model has been checked in previous works by means of the comparison with experimental results of static characteristics, small signal behaviour and noise performance of a 0.1  $\mu\text{m}$  gate AlInAs/InGaAs lattice matched HEMT (InP-based) [Mateos et al., 2000b].

### 2.1 Generalities

The basic philosophy of the single particle Monte Carlo technique, applied to charge transport in semiconductors, consist of simulating the motion of a charged carrier inside the

crystal. It is intended to study the free flight of the particle accelerated by an applied electric field between instantaneous random scattering events. Describing in more detail [Fig. 2(a)], the algorithm generates random free flight times for each particle, determines the state after each free flight, randomly chooses from amongst the different scattering mechanisms at the end of the free flight, computes the final energy and momentum of the particle after scattering, and finally reiterates the routine for the subsequent free flight. By monitoring the particle motion during the simulation, it is possible to statistically estimate the magnitude of several physical parameters for the particle such as the distribution function, average drift velocity, average energy, etc.

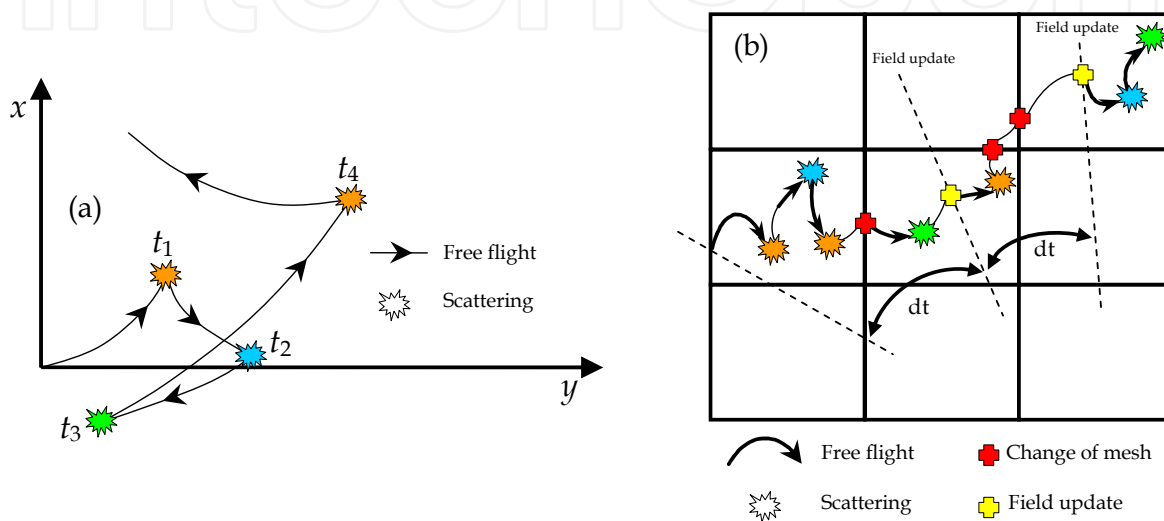


Fig. 2. (a) Simple diagram of the particle motion in the real space under a uniform electric field applied in the  $x$  direction. (b) 2D device simulator scheme.

In order to study transient behaviour, a synchronous simulation of a reasonable number of particles is indispensable. This is called *ensemble* Monte Carlo, in which the above algorithm is repeated for each particle. Every given time step in which, the individual carriers are simulated independent of the others, the quantities of interest are sampled and averaged. However, within a real semiconductor device, it is also essential to consider the internal electric potential obtained from the solution of the Poisson equation, as this is also an accelerating source for the particles. Consequently, it becomes necessary to couple both, the transport kernel, and the field solver to each other. For this purpose, a spatial grid is needed to solve the Poisson equation. In this frame, the simulation of the particle-based *ensemble* is carried out over a reasonably small time step, under the action of a self-consistent electric field (solution of Poisson equation) with the appropriate boundary conditions. At the end of each time interval, Poisson equation for the next time-step is solved again using the configuration of charges obtained from the *ensemble* Monte Carlo [Fig. 2(b)].

The electric field is computed (neglecting the inductive magnetic effects) by LU decomposition of the Poisson equation in a finite differences approach. Accurate scattering probabilities models for ionized impurity, alloy, polar and non-polar optical phonon, acoustic phonon and intervalley scattering ( $\Gamma$ -L-X) with a non-parabolic spherical valleys and effective mass approximation are used. As the size of our devices is larger than the de-Broglie electron wave length, quantum mechanical non-local effects are not taken into account. Neumann boundary conditions (the difference between the normal components of



the respective electric displacement vectors must be equal to any surface charge) are imposed in the semiconductor/dielectric boundaries, so that current only flows in/out of the device through the contacts, in which a Dirichlet condition (the potential is fixed) is imposed.

Concerning the analysis of noise, in the simulation we follow the standard scheme. The instantaneous current is calculated using the generalized Ramo-Shockley theorem [Kim et al., 1991], which evaluates the simultaneous contribution of all particles involved in the MC simulation to the total electrode current. The mathematical quantity employed for the characterization of noise is the autocorrelation function of current fluctuations. Then, by the Wiener-Kintchine theorem, the autocorrelation function is related to the noise spectra.

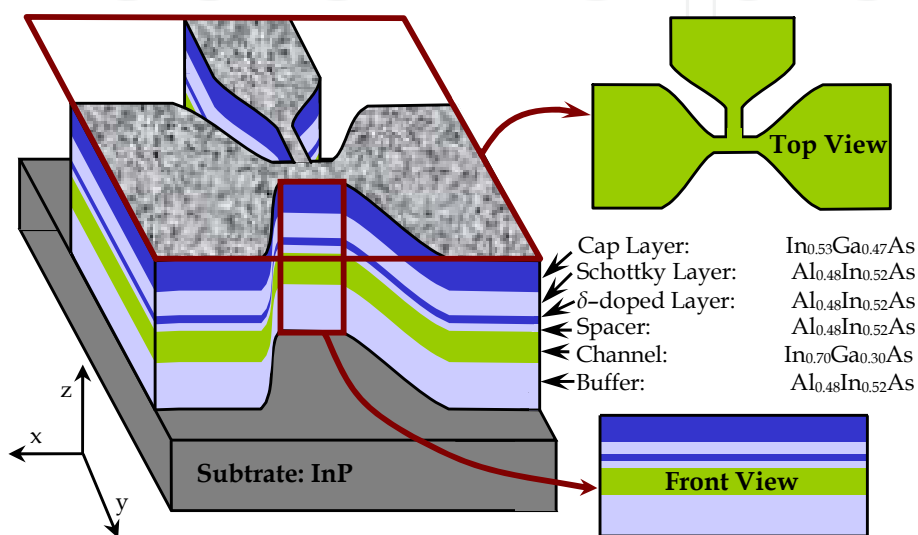


Fig. 3. Three-dimensional (3D) geometry and layer structure of a T-branch junction and scheme of the 2-D front-view (FV) and top view (TV) Monte Carlo simulations.

## 2.2 Simulations of channels: Three dimensional (3D) to two dimensional (2D) approach

For the correct modelling of nanodevices, a 3D simulation would be necessary in order to take into account the effect of the lateral surface charges and the real geometry of the structures. However, for the moment, only a 2D MC model has been developed, and some simplifications and assumptions must be made [Mateos et al., 2003a; Mateos et al., 2003b]. To account for the top geometry of the devices (for TBJs, YBJs, or ballistic diodes in our case), top-view (TV) simulations will be carried out [see Fig. 3]. They are performed in the  $xy$  plane; therefore, the real layer structure is not included, and only the channel will be simulated. In order to account for the fixed positive charges of the whole layer structure, a net doping  $N_{\text{db}}$  is assigned to the channel in TV simulations, but impurity scattering is switched off. In this way, the electron transport through the undoped channel is well reproduced, since this is a “virtual” doping  $N_{\text{db}}$  associated with the charges of the cap and  $\delta$ -doped layers. On the other hand, a negative surface charge density  $\sigma$  is assigned to the semiconductor-air interfaces to account for the influence of the surface states originated by the etching processes. The non-simulated dimension  $Z$  (used for the comparison of the simulated values of current with those measured in real devices) was estimated as  $Z = n_s / N_{\text{db}}$ , with  $n_s$  the value of sheet electron density in the fabricated channels. In addition, our approach has recently been further validated by the results of [Sadi et al., 2009]. Using a

3D model they have almost perfectly replicated the results obtained with our 2D model for the same set of TBJ junctions. Typically, InGaAs is the high-speed material used for the channel in the InP based heterojunctions. However, two different narrow band gap semiconductors, InAs and InSb, and their associated heterostructures, AlSb/InAs and AlInSb/InSb provide much higher values of mobility associated to their very small electron effective masses in the bottom of  $\Gamma$  valley (0.023 and 0.014 respectively). Our tool has been also properly adapted for these two high mobility semiconductors materials by carefully adjusting the simulation parameters in the single particle MC simulator. Experimental bulk mobilities have been reproduced by simulations:  $\mu=28000$  cm<sup>2</sup>/Vs for InAs and  $\mu=67000$  cm<sup>2</sup>/Vs for InSb [Rodilla et al., 2009].

### 2.3 Injection and physical model for the contacts

Since contact injection is a critical point when dealing with ballistic transport, the velocity distribution and time statistics of injected carriers will be accurately modelled [González & Pardo, 1996; González et al., 1999].

To compute the velocity distribution for the injected carrier,  $f_{iny}(\mathbf{v})$ , since the injected carriers are crossing the boundary between the contact and the adjacent cell inside the device, the thermal distribution,  $f_{th}(\mathbf{v})$ , should be weighted by the perpendicular velocity  $f_{iny}(\mathbf{v}) = \mathbf{v} \cdot f_{th}(\mathbf{v})$ . In this way, we account for the higher probability of particles with a large velocity to enter the device. In general the thermal distribution is the Fermi-Dirac (FD), however for non-degenerate material can be replaced by the Maxwell-Boltzmann one. A rejection method is used in case of FD because is not analytically integrable.

As concerns the time statistics, we first need to compute the number of carriers per unit of time entering in the device; which is the injection rate  $\Gamma$ . For a degenerate reservoir the injection statistics is a binomial distribution. However, for a non-degenerate reservoir, it is possible to use global Poissonian statistics in which the time between two consecutive electron injections,  $t_i$ , is generated with a probability per unit time  $P(t) = \Gamma e^{-\Gamma t}$ .

### 2.4 Surface charge modelling

The surface-to-volume ratio in nanoelectronic devices increases as the geometries are scaled down, so that, the device behaviour is more and more affected by the physical properties of the surfaces. Sidewall surface charge provokes the depletion of part of the conducting semiconductor channel as a consequence of coulombian repulsion and thus lowers the carrier density near the interface with the dielectric. In the total depletion approximation, the depletion width originated by a surface charge  $\sigma$  is  $W_d = \sigma / N_{db}$  at each side of the channel. Therefore, the effective conduction width is  $W_{eff} = W - 2W_d$ , with  $W$  the total width of the channel [Fig. 4(a)]. With the aim of extracting the experimental lateral depletion width  $W_d$ , the electrical characterization of channels with different length and width has been made. A value of  $W_d$  about 40 nm ( $\pm 10$  nm) for In<sub>0.7</sub>Ga<sub>0.3</sub>As channels [Galloo et al., 2004], corresponding in MC to a surface charge density of  $\sigma/q = (0.4 \pm 0.1) \times 10^{12}$  cm<sup>-2</sup> (using  $N_{db} = 10^{17}$  cm<sup>-3</sup>), has been obtained near equilibrium conditions.

A simple way to include the influence of this surface charge in MC simulations is to consider a model in which  $\sigma$  is fixed to the experimentally-extracted equilibrium value, and kept constant independently of the topology of the structure, position along the interface, bias and time. We will call this model as constant surface charge model. The surface charge is included as a Neumann boundary condition for the Poisson equation,  $\epsilon_2 E_2^n - \epsilon_1 E_1^n = \sigma$ ,

with  $\epsilon_i$  the permittivity and  $E_i^n$  the normal electric field in the  $i$ -th material. The applicability of this model becomes doubtful when the semiconductor becomes totally depleted (for  $W$  lower than 80 nm, so that  $W_{eff}$  becomes negative). Indeed, the physical origin of the surface charges is the trapping of electrons in surface states (located in the middle of the gap), but if the region near the surface is completely depleted, no electron would be able to reach the surface and the surface charge should decrease. In such a case ( $W_{eff} < 0$ ), if this model is used, the background doping  $N_{db}$  can not compensate the negative surface charge, charge neutrality is not ensured and unphysical high negative potentials are obtained in the simulation, providing incorrect results.

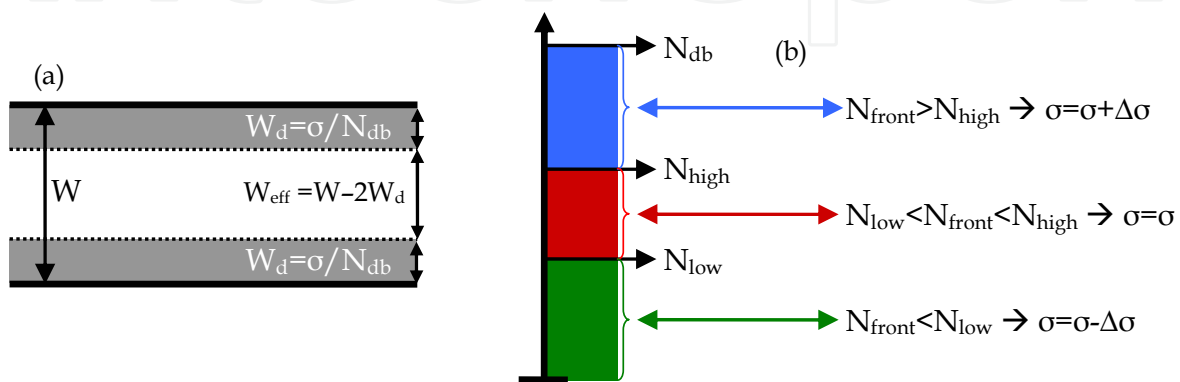


Fig. 4. (a) Effective channel width due to lateral depletion. (b) Surface charge self-consistent model.

Some features of the surface charges make difficult the possibility to implement them precisely in a MC simulator. The occupation of the surface states depends not only on its energy level but also on the potential profile and the Fermi energy in the surrounding region. Moreover, surface physical and chemical properties, fabrication processes, surface oxidation, composition and roughness determine the properties of the surface states and, as a consequence, the responses of nanometer scale devices. In addition, the capture and emission mean times of surface states (with values typically in the  $\mu s$  range) are much higher than scattering times, thus preventing their detailed treatment in a microscopic MC scheme, since a huge CPU-time would be necessary to take into account the correct dynamics of these states. For all these reasons, we have developed a new model [Íñiguez-de-la-Torre et al., 2007], based on the depletion induced by traps and not on their statistics, in which the local value of the surface charge is updated self-consistently with the carrier dynamics near the interface during the simulation. This model so called self-consistent charge model completes and improves the previous works where a constant surface charge density (neither depending on the position nor on the applied potential) was considered at the semiconductor-dielectric interfaces associated with the presence of surface states.

The philosophy of our new self-consistent model is based on the adaptation of the value of the surface charge to the carrier density in the nearby region [Fig. 4(b)]. First, we evaluate the carrier concentration next to the boundary ( $N_{front}$ ) as an average over a given number of iterations  $N_i$ . Then, it is checked if  $N_{front}$  has a value in the range  $[N_{low}, N_{high}]$  which represent the limits to which we try to adapt the electron concentration next to the interface. If the concentration ( $N_{front}$ ) is higher than the upper limit ( $N_{high}$ ), we increase the surface charge in a given amount  $\Delta\sigma$ , so that its repulsive effect provokes stronger channel depletion



and thus the concentration should diminish. On the other hand if  $N_{\text{front}}$  is smaller than the lower limit ( $N_{\text{low}}$ ), the surface charge is decreased in the same density  $\Delta\sigma$  to reduce the (too large) induced depletion. The choice of the limits  $N_{\text{low}}$ ,  $N_{\text{high}}$  is constrained by the level of statistical resolution achievable by the simulation (which depends on the number of simulated electrons). If the lower limit is too low (the forced depletion level is too strong), below the value of electron concentration that MC simulations can reliably estimate, wrong results would be obtained. More details of the values of the parameters can be found in [Iñiguez-de-la-Torre et al., 2007].

To conclude, it is important to remark that evidently this “ad-hoc” surface charge model is not able to reproduce the statistics of occupation of surface states, but it does describe correctly the global effect of the surface charge. We will apply this self-consistent model to study T-shaped three-terminal ballistic junctions (TBJs) based on InAlAs/InGaAs layers and compare the results with experimental measurements, achieving a satisfactory agreement.

### 3. Three-branch junctions

The device structure of the Three-Branch Junction (TBJ) is very simple. The TBJ is a three-terminal device consisting of a T-shape (or Y-shape) conductor with three contacts at the end of each branch. The conductor is typically made of a 2DEG formed in a modulation-doped heterostructure wafer. Employing high resolution resins, electron-beam lithography and dry or wet etching, the 2DEG wafer is patterned into a T-or Y-shape structure with a dimension comparable to the mean free path ( $l_m \sim 100\text{-}300\text{ nm}$ ) at RT [Cappy et al., 2005].

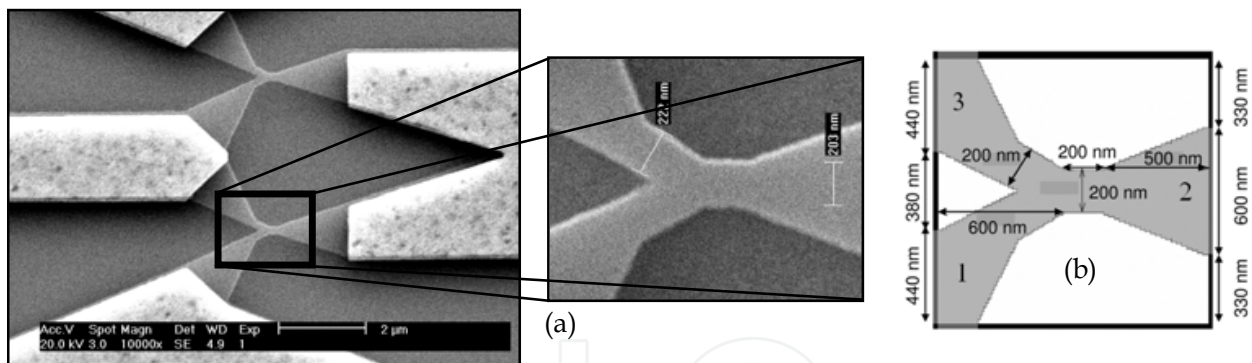


Fig. 5. (a) SEM image of a double Y-Branch junction topology with coplanar waveguide (CPW) accesses. (b) Top-view geometry (sizes correspond to the real YBJ) used in the MC simulations.

Figure 5(a) shows a scanning electron microscopy (SEM) image of a typical device structure. Bright regions and dark regions indicate 2DEG layer and etched away material respectively. We also see the accesses connecting the Y-shape structure with the ohmic contacts and metal interconnects pads for DC probing (or are a part of planar transmission lines for high-frequency measurements [Irie et al., 2010]). Figure 5(b) is a screenshot of our MC tool.

#### 3.1 Overview and working principle

TBJs operation is described as follows. Input voltages are applied to the L- and R-terminals, while the C- terminal is used as the output terminal. In big devices, where  $l_m$  is smaller than the distance between contacts, each branch can be represented by a resistance [Fig. 6(a)]. So,

if we apply two separate potentials with opposite sign to the right and left terminals (push-pull fashion), the potential in the middle of the junction is zero. In this ohmic transport regime, the potential measured at the bottom of the open-circuited central branch (stem),  $V_C$ , is also zero [Fig. 6(c)]. However, when the lengths of the branches,  $L$ , are smaller than  $l_m$ , transport can not be anymore considered diffusive, but ballistic or quasiballistic. In this regime, the horizontal branches can be understood as non-linear resistances  $R(V)$ , Fig. 6(b), and; as shown by the experiments [Shorubalko et al., 2001] and theory [Xu, 2001],  $V_C$  is always negative and presents a quadratic down-bending shape  $V_C = -\alpha V^2$ , Fig. 6(c). The non-linear effect can be enhanced by decreasing the temperature of operation because the reduction in the number of scattering mechanisms [Irie et al., 2008].

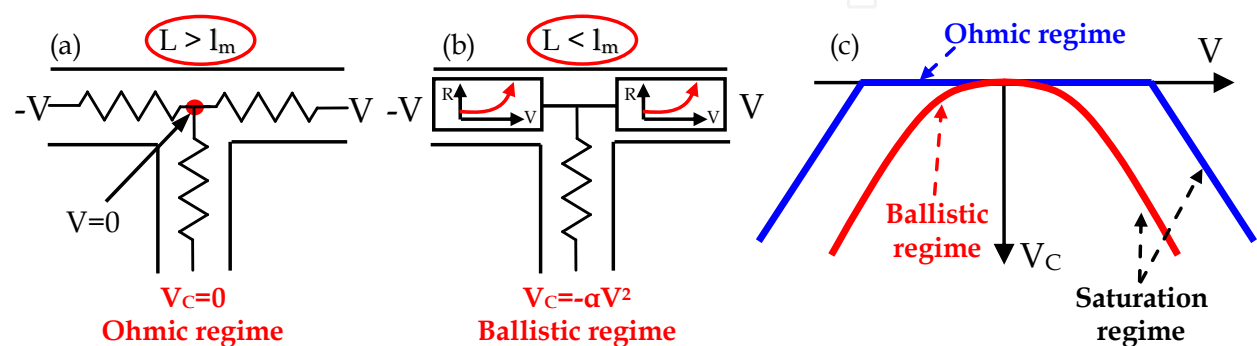


Fig. 6. Sketch of the (a) ohmic and (b) ballistic regimes of transport in TBJs and the (c)  $V_C$  response for both types of transport.

The negative values of  $V_C$  have been reproduced by Monte Carlo simulations of TBJs [Fig. 7(a)]. The explanation is related to space-charge effects originated by the joint action of (i) the surface charge at the semiconductor-air interfaces, (ii) the background positive fixed charge  $N_{db}$ , and (iii) the inhomogeneous charge distribution associated with the ballistic motion of carriers injected at the contacts. The different resistance of the left and right branches due to the asymmetric profile of electron concentration along the horizontal branches, being higher near the negative electrode [Fig. 7(c)], is the consequence of the above effects. The surface charge lowers the electric potential when moving away from the contacts provoking the progressive depletion of the channel, thus leading to the typical minimum of potential and concentration in the middle of the structure, characteristic of space charge limited conditions [Fig. 7(d)]. When the TBJ is biased, the concentration shows an asymmetric shape (higher near the negative electrode due to the electron ballistic motion) leading to a shift of the potential minimum towards the negative electrode. As a consequence, the potential at the centre of the longitudinal channel is always negative (increasing with larger  $V$ ) and propagates to the bottom of the vertical branch, thus leading to the characteristic bell-shaped values of  $V_C$ . It is to be noted that we are using the constant surface charge model. In Fig. 7(a), we can also observe that the negative values of  $V_C$  reach a maximum for an intermediate value of  $\sigma$ , just when the width of the channel coincides with the lateral depletion induced by the surface charge (for  $\sigma/q = 0.25 \times 10^{12} \text{ cm}^{-2}$ ,  $W_d = 25 \text{ nm}$ , and the theoretical effective width of the channel  $W_{eff} = W - 2W_d$  becomes 0). In the next section we show how the self-consistent surface charge model (explained in section 2.4) introduce an extra asymmetry in the concentration leading to more negative values of  $V_C$ .

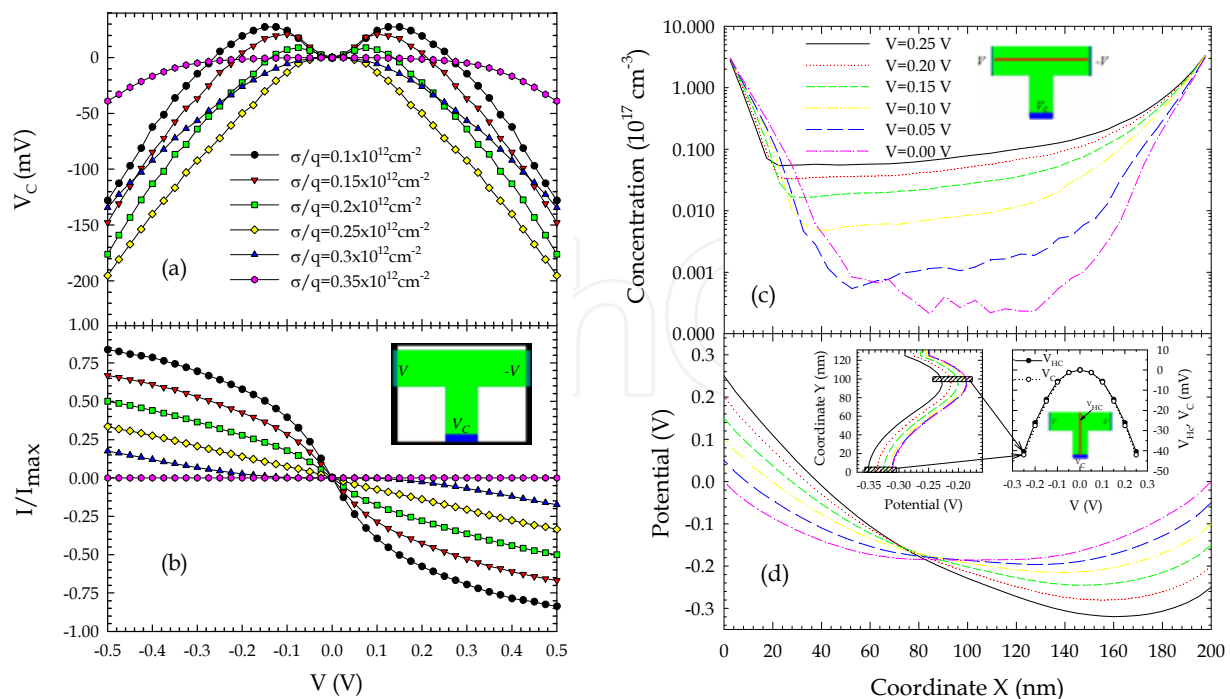


Fig. 7. (a) Electric potential at the bottom of the central branch of the TBJ and (b) normalized horizontal current when simulating with a constant surface charge model for different values. The inset shows the geometry of the TBJ with 50-nm-wide and 75-nm-long branches. (c) Horizontal electron concentration and (d) electric potential profiles of the TBJ for different bias conditions. The insets show the vertical potential profile in the middle of the central branch for several biasing, and the values of the potential at the bottom of this branch  $V_C$  and at the centre of the junction  $V_{\text{HC}}$  as a function of  $V$ .

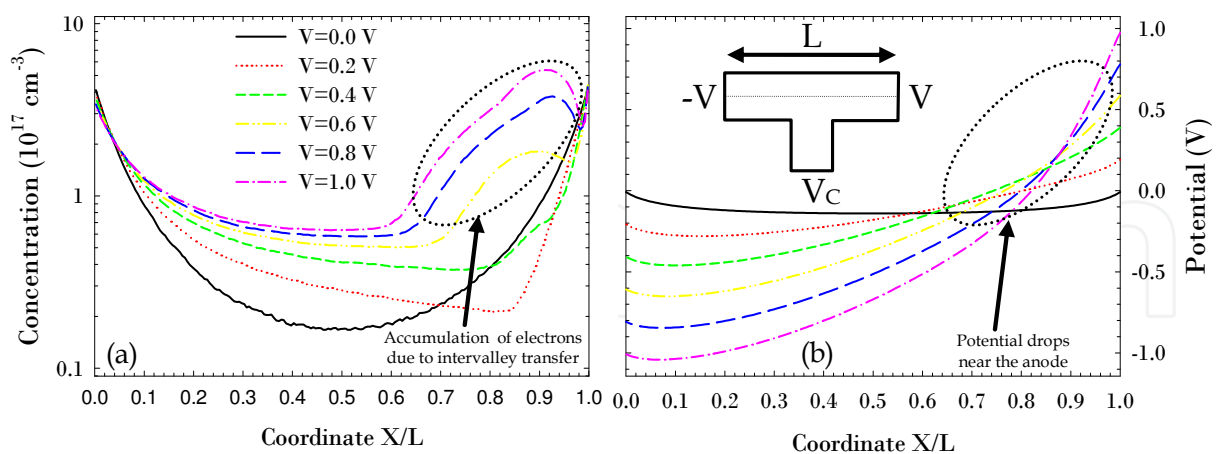


Fig. 8. (a) Profiles of electron concentration and (b) electric potential along the horizontal branch of the TBJ.

It is important to remark that, as sketched in Fig. 6(c), when increasing the bias ( $V > 0.25 \text{ V} \approx \Delta E_{\text{IL}}/2e$ ), even in the ballistic TBJs, the response of  $V_C$  becomes linear with  $V$  due to the appearance of  $\Gamma$ -L intervalley scattering mechanisms. That leads to the emergence of an accumulation domain near the positive electrode [Fig. 8(a)] completely screening the

variation of the potential drop between the central branch and the negative electrode [Fig. 8(b)]. This mechanism is also responsible for the saturation of the current [Fig. 7(b)] and the surprising negative values of  $V_C$  (since they are expected to be ohmic) measured in large TBJs [Mateos et al., 2004; Irie et al., 2008].

### 3.2 Self-consistent surface charge model. Stem width

As showed in experiments and contrary to the expectations, the central branch is not exactly a potential probe which measures the potential at the middle of the TBJ and therefore  $V_C$  depends on the stem width [Íñiguez-de-la-Torre et al., 2007]. Five TBJs with different widths of the vertical branch,  $W_{\text{VER}}=66, 78, 84, 94$  and  $108$  nm, have been fabricated and simulated in our MC tool with the self-consistent charge model (explained in section 2.4). Fig. 9(a) shows the MC values of  $V_C$  and the current  $I$  flowing through the horizontal branches in the TBJs when biased in push-pull fashion. The parabolic behaviour of  $V_C$  is strengthened when reducing the width of the vertical branch. This is in principle an unexpected result, since the vertical branch was believed to be only a measure (passive) element, in such manner that the value of  $V_C$  should be independent of its width  $W_{\text{VER}}$ . The inset of Fig. 9(a) shows how, as expected, the current is independent of  $W_{\text{VER}}$ , since the horizontal branch is identical for the different TBJs. The calculations performed with MC are consistent with the experimental results showing the same trend and a satisfactory quantitative agreement [Íñiguez-de-la-Torre et al., 2007].

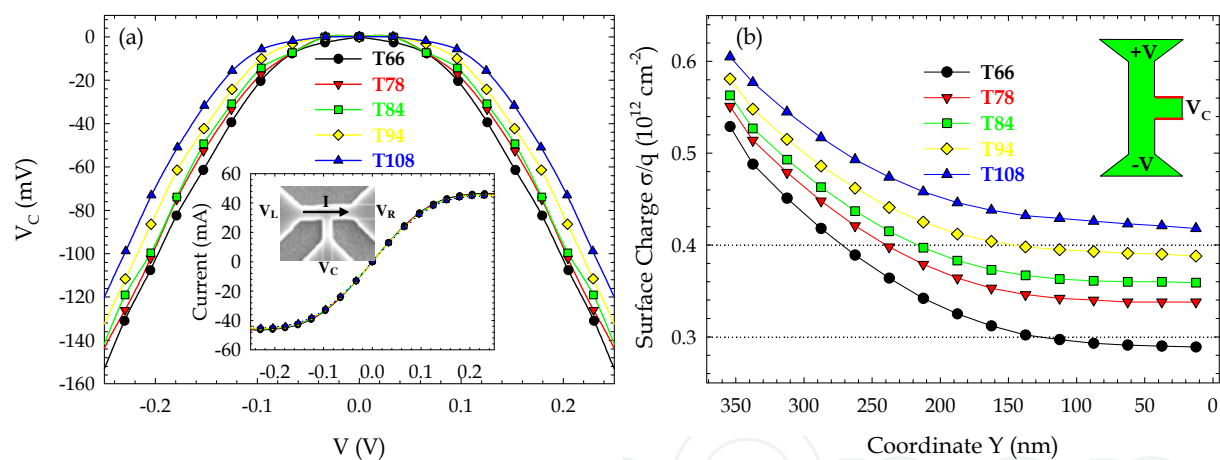


Fig. 9. (a) MC values of the bottom potential  $V_C$  and current (inset) in the TBJ junctions with 66, 78, 84, 94 and 108 nm wide vertical branches (denoted as T66, T78, T84, T94 and T108, respectively) as a function of the push-pull bias  $V$ . (b) Surface charges in the sidewalls of the vertical branch under equilibrium conditions ( $V=0$ ).

The proposed self-consistent surface charge model allows for the variation of the surface charge  $\sigma$  along the position in the interface in accordance with the surrounding free carrier concentration. This possibility of self-adaptation permits the surface charge in the narrowest junction (called T66) to reach values that approximately cause total depletion of the vertical branch,  $\sigma/q=0.3 \times 10^{12} \text{ cm}^{-2}$ . In contrast, in the widest junction (called T108) the surface charge is limited by a value close to that obtained in the experimental measurements,  $\sigma/q=(0.4 \pm 0.1) \times 10^{12} \text{ cm}^{-2}$  [Fig. 9(b)]. Furthermore, the surface charges take a value practically constant near the bottom of the vertical branch, which indicates that the results will not change if this branch is made longer.



In previous works, within the constant charge model, the vertical branch was considered as a voltage probe, providing at its bottom ( $V_C$ ) the variations of  $V_{HC}$  (potential at the centre of the horizontal branch) [inset 7(d)]. However, within the self-consistent model, the surface charge at the sidewalls of the vertical branch and the carrier penetration inside it change with the bias (like in Y-Junctions), which provokes that  $V_C$  is no longer a faithful reflection of the  $V_{HC}$  variations and it is necessary to consider the electric potential difference  $\Delta V_V$  between  $V_C$  and  $V_{HC}$ , which is not equal for all the biasing. Therefore, the values of  $V_C$  can be considered as the result of two combined effects: a horizontal one (given by  $V_{HC}$ ) and a vertical one (given by  $\Delta V_V$ ).

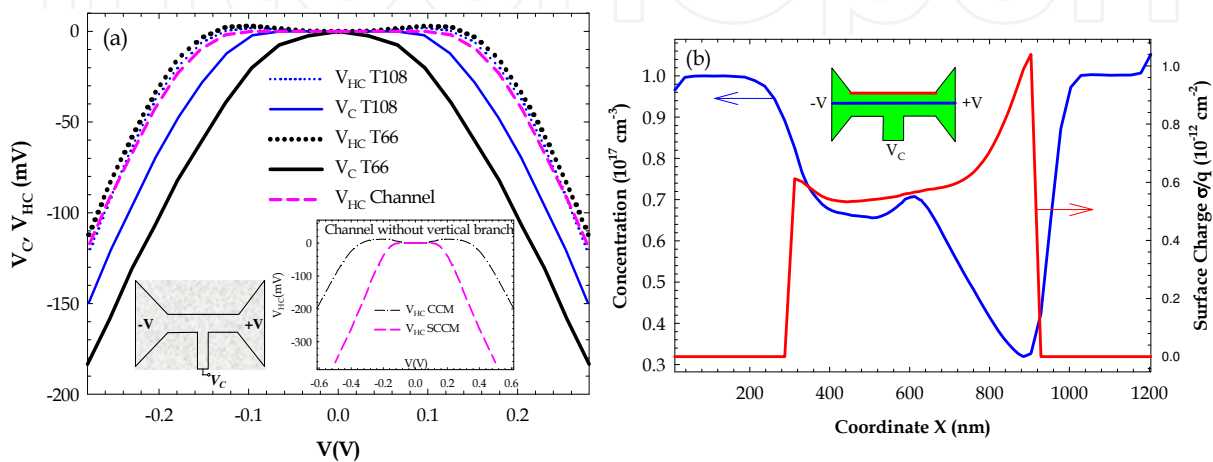


Fig. 10. (a)  $V_{HC}$  and  $V_C$  as a function of the applied voltage for the TBJs with  $W_{VER}=66$  and  $108$  nm.  $V_{HC}$  for a channel without the vertical branch is also plotted for comparison. The inset shows  $V_{HC}$  calculated in the channel without the vertical branch with the constant charge model ( $\sigma/q=0.4 \times 10^{12} \text{ cm}^{-2}$ ) and self-consistent charge model. (b) Profiles of carrier concentration along the centre of the horizontal branch and surface charge along the top boundary of the T66 for  $V=V_R=-V_L=0.25$  V.

We analyze the horizontal effect, that is, the values of  $V_{HC}$ . In Fig. 10(a) we plot the values obtained with the MC simulations for  $V_{HC}$  in T66 and T108, together with those calculated in a channel without vertical branch. It can be observed that, as expected, the values of  $V_{HC}$  practically coincide in the three structures (transport takes place in horizontal direction and the width and length of the horizontal branch are practically the same). The inset of Fig. 10(a) also compares the values of  $V_{HC}$  in a simple channel (without vertical branch) obtained with the constant and self-consistent charge models. The self-consistent model leads to a considerable enhancement of the negative values of  $V_{HC}$ , which is the signature of an enhanced electron charge asymmetry in the horizontal direction, especially for high biasing, as can be shown in Fig. 10(b) for  $V=0.25$  V. A strong depletion of carriers takes place at the anode side of the horizontal branch. This region becomes highly resistive, so that most of the applied potential drops here and leads to the high negative values of  $V_{HC}$ . The origin of the increase of the surface charge with the applied voltage near the anode lies in the fact that, due to the ballistic motion of electrons, their longitudinal energy increases significantly as they approach the right contact. Scattering mechanisms, even if there are very few, produce some energy redistribution, and thus make the transversal energy component also increase. In this way electrons are able to approach the boundaries of the TBJ (in spite of the repulsive effect of the surface charge) and contribute to raise the value of  $\sigma$ .



### 3.3 Influence of the horizontal branch

Our self-consistent surface charge model can also be applied to explain the behaviour when the length  $L_{\text{HOR}}$  and the width  $W_{\text{HOR}}$  of the horizontal branches are modified [Fig. 11]. When the length of the horizontal branches  $L_{\text{HOR}}$  is changed we found that the values of  $V_{\text{HC}}$  are very similar for all the structures. This is due to the analogous horizontal concentration profiles found for the different lengths. As in the previous TBJs, it is the presence of the vertical branch and the associated surface charges which leads to different values of  $V_{\text{C}}$  in each of the structures. Like in the case of the experimental results [Irie et al., 2008] we found that the down-bending behaviour of  $V_{\text{C}}$  is stronger for shorter junctions. This result is expected because of the more ballistic character of transport in shorter structures, but our results indicate that surface charges and the presence of the vertical branch also play a role.

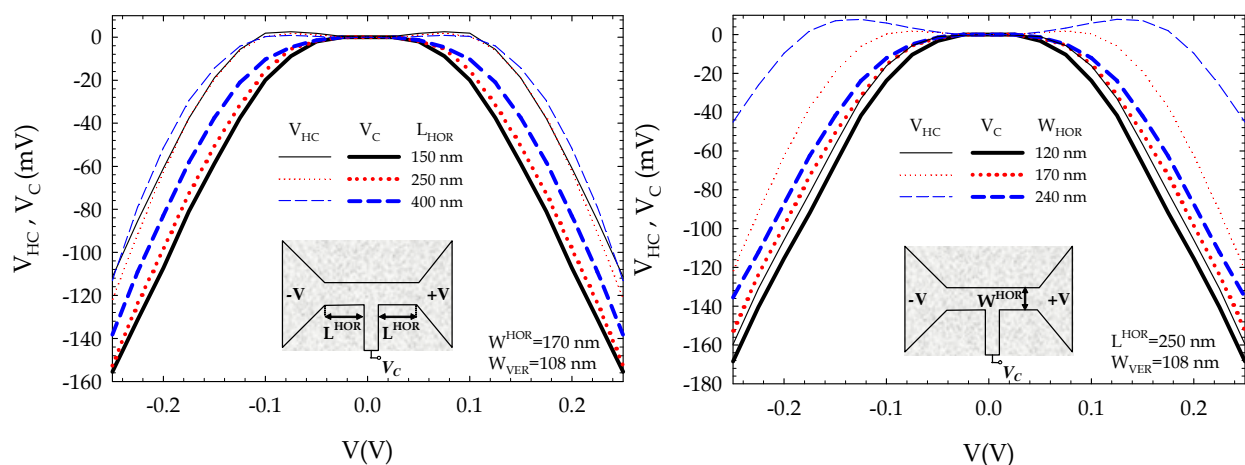


Fig. 11. (a)  $V_{\text{HC}}-V$  and  $V_{\text{C}}-V$  for TBJs with  $L_{\text{HOR}}=150, 250,$  and  $400$  nm. (b)  $V_{\text{HC}}-V$  and  $V_{\text{C}}-V$  for TBJs with  $W_{\text{HOR}}=120, 170,$  and  $240$  nm.

Concerning the width of the horizontal branch  $W_{\text{HOR}}$ , the values of  $V_{\text{C}}$  are higher (more negative) as the width is decreased, in accordance with the trend found in our experiments [Íñiguez-de-la-Torre et al., 2009a]. However, since the length is identical, the origin must be related not only to ballistic transport. Results can be interpreted in terms of a new factor: the strength of surface charge effects. Remarkably, and in contrast with the behaviour found when modifying  $W_{\text{VER}}$  and  $L_{\text{HOR}}$ , in this case the values of the potential at the centre of the junction  $V_{\text{HC}}$  exhibit a strong dependence on  $W_{\text{HOR}}$ . The narrower the horizontal branch, the lower the free carrier concentration due to the stronger depletion induced by the enhanced surface charge. For this reason the horizontal potential profile is different in each junction and also the value of  $V_{\text{HC}}$ . The dependence of  $V_{\text{HC}}$  on  $W_{\text{HOR}}$  is smoothed in the bottom potential  $V_{\text{C}}$  by surface charge adaptation in the vertical branch as explained in the previous section. Therefore, it is the role played by surface charge and the associated depletion what leads to the observed variations between structures with different  $W_{\text{HOR}}$ . The surface charge influence on  $V_{\text{C}}$  is much stronger than that of ballistic transport in the case of small  $W_{\text{HOR}}$ , but decays sharply for wide TBJs in agreement with the experimental findings [Íñiguez-de-la-Torre et al., 2009a]. Finally we want to remark that in the wider TBJs, for the lowest applied voltages,  $V_{\text{HC}}$  gets slightly positive values before becoming negative. MC microscopic results indicate that under such bias conditions the branch contacted to the cathode is more resistive than the anode one providing these positive values. It is due to a

velocity overshoot effect (more pronounced near the cathode) taking place for weak enough surface charge effects.

Overall, we can conclude that the parabolic response (associated with ballistic transport) sharply decreases for larger  $L_{HOR}$ , and increases in efficiency for narrower channels ( $W_{VER}$  and  $W_{HOR}$ ). Experiments also shown an unexpected significant degree of ballistic transport even in TBJs with  $L_{HOR}=2 \mu\text{m} \gg l_m$  [Irie et al., 2008] and  $W_{HOR}=2 \mu\text{m}$  [Íñiguez-de-la-Torre et al., 2009a]. This robustness of the TBJs nonlinear response is a unique advantage in terms of realizing a room-temperature integrated circuitry using TBJs over a wide range of channel sizes.

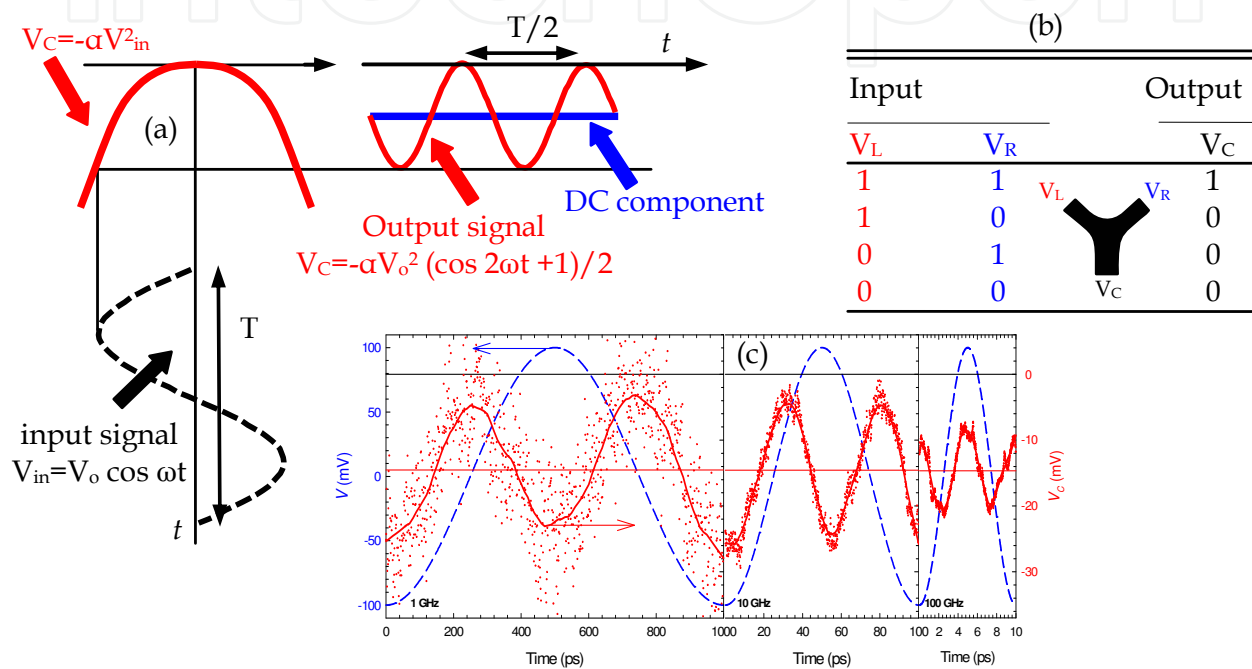


Fig. 12. (a) Illustration of detection and frequency doubling of RF signals in TBJs, (b) logic truth table for a symmetric TBJ device, operated as an AND gate, when defining positive voltage as the binary value of 1 and (c) MC time domain simulation of a TBJ for different frequencies of a push-pull input signal of amplitude 100 mV: 1, 10 and 100 GHz.

### 3.4 Rectification and doubling in TBJs

The nonlinear response of TBJs can be exploited to perform several analog and digital functions as illustrated in Fig. 12. An example is high-frequency signal rectification [Bednarz et al., 2005] and second-harmonic generation [Lewén et al., 2002]. Frequency mixing, doubling and phase detection have also been demonstrated [Shorubalko et al., 2002; Sun et al., 2007; Gardès et al., 2008]. Another example of application is as logic gate for digital electronics [Rahman et al., 2009]. It is clear, for example [Fig. 12 (b)], that if we use left and right branches as inputs, the central branch output will perform the logic AND operation ( $V_C$  has high voltage only when both  $V_L$  and  $V_R$  are high and low voltage in other cases) [Xu, 2002]. It was reported that with more complicated structures of several TBJs can work as NAND [Reitzenstein et al., 2002, Xu et al., 2004], NOR [Müller et al., 2007], half adder [Worschech et al., 2003; Reitzenstein et al., 2004], full adder [Lau et al., 2006] or SR latch [Sun et al., 2008], etc.

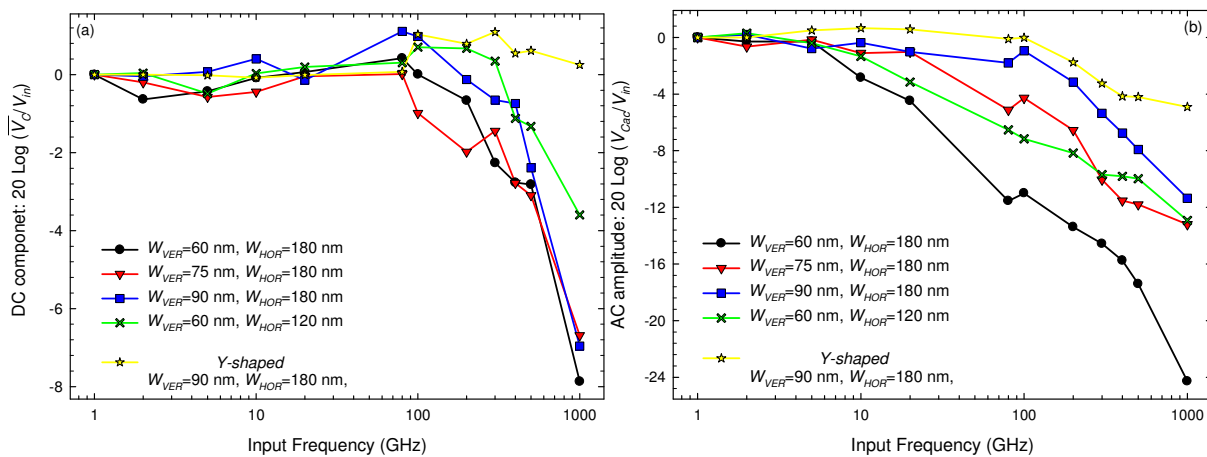


Fig. 13. Frequency dependence of (a) amplitude,  $V_{Cac}$  and (b) average DC value,  $\overline{V_C}$ , of the response of  $V_C$  (normalized to the input amplitude and in dB) to signals of amplitude 100 mV applied in push-pull to the inputs in T-shaped junctions with different  $W_{VER}$  and  $W_{HOR}$  and in a Y-shaped junction. For a better comparison, the low-frequency value has been subtracted to each curve.

In this section we study the effect of the geometry ( $W_{HOR}$ ,  $W_{VER}$ ) and shape on the performance of three-branch junctions operating as detectors and frequency doublers [Fig. 12(a)]. To this end, we apply 100 mV sinusoidal signals in push-pull fashion. In Fig. 12(c) the time domain evolution of the stem output voltage  $V_C$  is represented when the frequency of the input signal is 1, 10 and 100 GHz. It can be observed that the device has an excellent performance as frequency doubler at least up to 100 GHz. Fig. 13 shows the values for the amplitude,  $V_{Cac}$  and the average DC value  $\overline{V_C}$  of the response of  $V_C$ , as a function of frequency for the different simulated junctions (for the sake of clarity the low-frequency value has been subtracted). As a general feature, the cut-off for  $V_{Cac}$  appears at much lower frequencies than for the mean value,  $\overline{V_C}$ , taking place around 1 THz [Fig. 13(a)]. For the T-shaped junctions as the value of  $\overline{V_C}$  is mainly related to the electron horizontal transport, its cut-off is hardly influenced by the width of the vertical branch. On the other hand,  $V_{Cac}$  is controlled by the penetration of carriers into the stem, so that its width ( $W_{VER}$ ) clearly changes its cut-off frequency (higher frequencies for wider stems, in which carriers enter more easily). Nevertheless, wider stems provide less negative values of  $V_C$  at low-frequency. As a consequence, for an optimized response  $W_{VER}$  must be chosen depending on the required type of operation and frequency. On the other hand, when reducing  $W_{HOR}$ , a slight increase of the cut-off frequency is observed in both quantities; however, the matching to the typical 50  $\Omega$  lines would be worse due to the higher impedance of the TBJ. Concerning the shape, the Y geometry much improves the global performance of the device as a result of an enhanced vertical electric field and a stronger injection of carriers into the stem (having a more pronounced influence on the cut-off of  $V_{Cac}$ , associated with frequency doubling applications). Moreover, better performances are expected if the angle between left and right branches of the junction is further decreased.

It is to be noted that in these high-frequency MC simulations the profile of the surface charge is frozen to that previously calculated under equilibrium conditions, since the typical capture/emission times of the surface states are about 1  $\mu$ s, several orders of magnitude longer than the maximum period used for exciting the junctions (1 ns). In fact, a low

frequency plateau should be observed in experiments with a cut-off corresponding to the inverse characteristic lifetime of the surface charge traps.

#### 4. Self-switching diodes

The second nanometer-scale nonlinear device that we study in detail in this chapter was proposed in 2003 by A. M. Song and named Self-Switching Diode. The key point in the fabrication of the device is the etching of the two L-shaped insulating grooves defining a narrow semiconductor channel [Fig. 1(b)]. An applied voltage  $V$  not only changes the potential profile along the channel direction, but also either widens or narrows the effective channel depending on the sign of  $V$ . This results in a diode-like characteristic, but without the use of any doping junction or barrier structure.

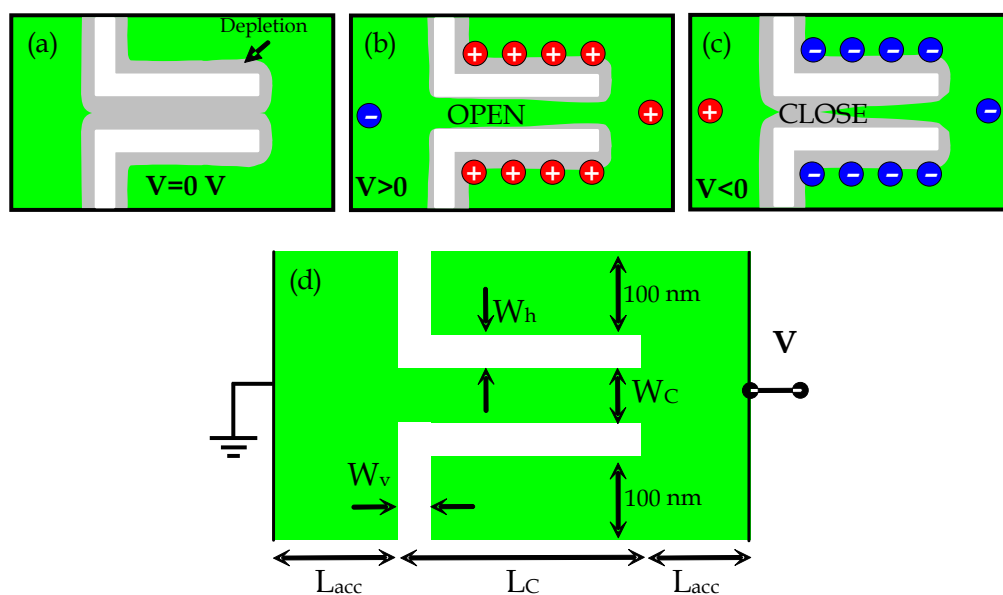


Fig. 14. (a) Depletion region formed close to the etched boundaries in equilibrium. Depending on the sign of the applied voltage the effective channel width will (b) increase or (c) reduce. (d) SSD geometry for the MC simulations.

The two-terminal structure allows SSD-based circuits to be realized by a simple single step lithographic process, so that its size can be easily reduced to the nanometer-range. Thus, by using fast III-V materials, the high frequency performance of SSDs can be dramatically boosted thanks to a much shorter transit time, due not only to a smaller channel length but also to an enhanced electron velocity associated to ballistic transport. And last but not least, the planar geometry of the SSDs allows placing the two contacts with long separation, so that parasitic crosstalk capacitances can be drastically reduced. These facts, together with the intrinsically high electron velocity channels, should permit the fabrication of SSDs working in the THz range.

##### 4.1 Overview, working principle and I-V curves

The voltage applied to the anode (right contact) of the SSD propagates to the vicinity of the channel, while in the cathode region (at the left of the trenches) the potential is always essentially zero. In equilibrium, the channel is closed due to the depletion induced by the

surface charges located at the lateral walls [Fig. 14(a)], which lead to the appearance of a longitudinal potential barrier. When  $V > 0$ , the positive voltage reaches the lateral regions of the SSD channel, so that the potential barrier is lowered (or even removed), thus allowing the electron flow (the channel is open) [Fig. 14(b)]. On the contrary, when  $V < 0$ , the potential profile in the right part of the device is almost unchanged with respect to the equilibrium situation (it is just shifted to lower values), the channel thus remaining closed [Fig. 14(c)].

We analyze I-V curves, noise spectra and rectification when some parameters of the diode geometry are modified (keeping the others constant). The reference SSD for all the simulations will be the one with:  $W_C = 50$  nm,  $L_C = 250$  nm,  $W_h = W_v = 5$  nm and  $L_{acc} = 175$  nm. In general terms the forward current shows an exponential dependence on the applied voltage for low values of  $V$  (as long as the barrier is present), and then becomes linear (resistive behaviour), with a tendency to saturation at the highest applied voltages due to hot-carrier effects [insets Fig. 16].

For devices with smaller channel width,  $W_C$ , inset Fig. 16(a), the turn-on voltage is larger due to a larger barrier at equilibrium, which needs a higher applied voltage to disappear. The length of the channel,  $L_C$ , is also found to largely influence the device behaviour. As observed in the inset of Fig. 16(b), short-channel effects appear when the aspect ratio of the channel ( $L_C/W_C$ ) decreases. In such a case, under reverse bias, the potential of the lateral regions is not able to deplete the channel, so that the barrier preventing the current flow disappears and an inverse leakage current flows (as observed for  $L_C = 100$  nm). The very thin trenches of the devices not only prevent the presence of inverse leakage current for very short channels (it only appears for  $L_C = 100$  nm), but also the forward current is much improved, inset Fig. 16(c). As observed in the inset of Fig. 16(c) and Fig. 16(d), the turn-on voltage is influenced by the width of the horizontal (and not by the vertical) trenches, decreasing for smaller  $W_h$ . This is due to the stronger transverse electric field present for smaller  $W_h$ , which enables a more efficient control of the opening and closing of the nanochannel when biasing the anode.

Therefore, the operation principle of this device is similar to that of an enhanced mode field effect transistor (pinched off at equilibrium) in which lateral gates (in this case short circuited to the drain) control the current flow through the channel. From the point of view of applications, the non-linear response of the diodes and the ultra fast ballistic transport opens the possibility of fabricating circuits for rectification, detection or even harmonic generation at very high frequencies.

#### 4.2 Noise spectra

By downscaling the device dimensions, the detection properties of an array of SSDs has been proved up to 110 GHz at RT [Balocco et al., 2005] and up to 2.5 THz at 10 K [Balocco et al., 2008]. At so high frequencies, the intrinsic noise generated by the diodes becomes a performance limitation, and must be carefully analyzed in order to reduce its level as much as possible. Initial studies [Íñiguez-de-la-Torre et al., 2008] of the spectral density of current fluctuations at low-frequency  $S_I(0)$  (in the plateau beyond the  $1/f$  range) compared to the  $2qI$  value (with  $q$  the electron charge) have evidence the presence of full shot noise not only under inverse but also under direct bias below a certain threshold potential, above which the level of noise is lower than  $2qI$  [Fig. 15(a)]. Full shot noise (both under forward and reverse bias) appears when the transport is barrier controlled and the current is provided by uncorrelated carriers surpassing the barrier. The noise temperature is close to half the value



of the lattice temperature associated with an ideal exponential dependence of the forward current, which usually goes along with the previously commented full shot-noise behaviour. At high forward bias the barrier is lowered or even disappears, the channel resistance decreases, and the diffusive accesses to the channel become more important and the noise temperature increases significantly over the lattice temperature due to a strong electron heating.

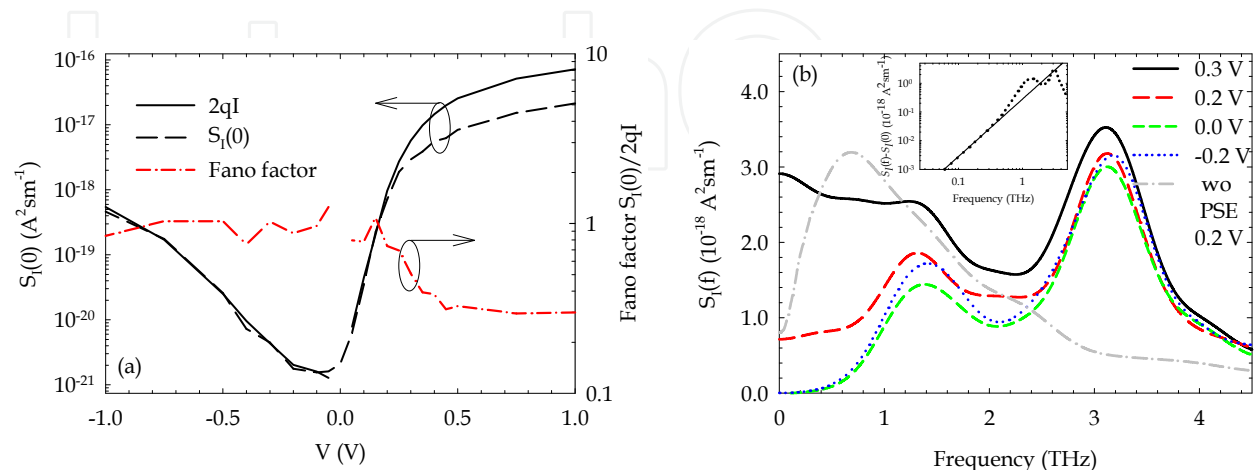


Fig. 15. (a) MC values of  $S_I(0)$ , compared to  $2qI$ , as a function of the applied voltage (left axis). The Fano factor  $S_I(0)/2qI$  is also plotted (right axis). The inset shows the I-V curve of the diode in linear scale. (b)  $S_I(f)$  for several bias conditions in the reference SSD. The case in which the PS is switched off is also shown for  $V=0.2$  V. The inset illustrates the  $f^2$  dependence of the noise spectrum for  $V=0.0$  V. Reference SSD.

For high frequency the current noise spectra  $S_I(f)$  for the reference SSD is shown in the Figure 15(b). Two main peaks are observed in the spectra. 3D plasma oscillations are at the origin of the one appearing at the highest frequencies (above 3 THz). When the PS is switched off plasma oscillations are not present and this peak disappears. The other peak, between 1-2 THz, is attributed to returning-carrier effects taking place in the space-charge regions originated by the surface charge at both sides of the vertical trenches. It exhibits the characteristic  $f^2$  behaviour [inset of Figure 15(b)] already found in other devices like Schottky-barrier diodes, revealing a capacitive coupling of the returning carrier fluctuations to the noise at the terminals. But more interesting, and in contrast with the other peak, the frequency of this one depends on the geometry of the SSD as we can see in Figure 16.

As observed, the level of noise at high frequency is higher the larger is the impedance of the accesses as compared to that of the channel. This explains, for example, why  $S_I(f)$  is higher when decreasing  $L_C$  or increasing  $W_C$  or  $L_{acc}$ , while it remains with similar amplitude when changing  $W_h$  or  $W_v$ . The increase of  $S_I(f)$  originated by the peak at lower frequency could limit the frequency range of potential applications. Thus, a first possibility to reduce the noise related to the returning-carriers peak is to decrease the resistance of the accesses relative to that of the channel. The best choice to this end is shortening  $L_{acc}$  [see Fig. 16(e)], which is always desirable to reduce parasitic resistances but may increase the parasitic capacitance between electrodes. Decreasing  $W_C$ , Fig. 16(a), or increasing  $L_C$ ; Fig. 16(b), would enhance the channel resistance and reduce the current level, both undesirable effects. Moreover, a longer channel leads to lower cut-off frequency. A second possibility is to try to move the peak to higher frequencies, thus reducing the amplitude of the noise in the range

of interest (around 1 THz). As observed in Fig. 16, by modifying  $W_C$ ,  $L_C$  or  $L_{acc}$ , the frequency of the maximum hardly changes. In contrast, an increase in the width of the vertical trenches  $W_v$ , shifts the peak to higher frequencies, Fig. 16(d).

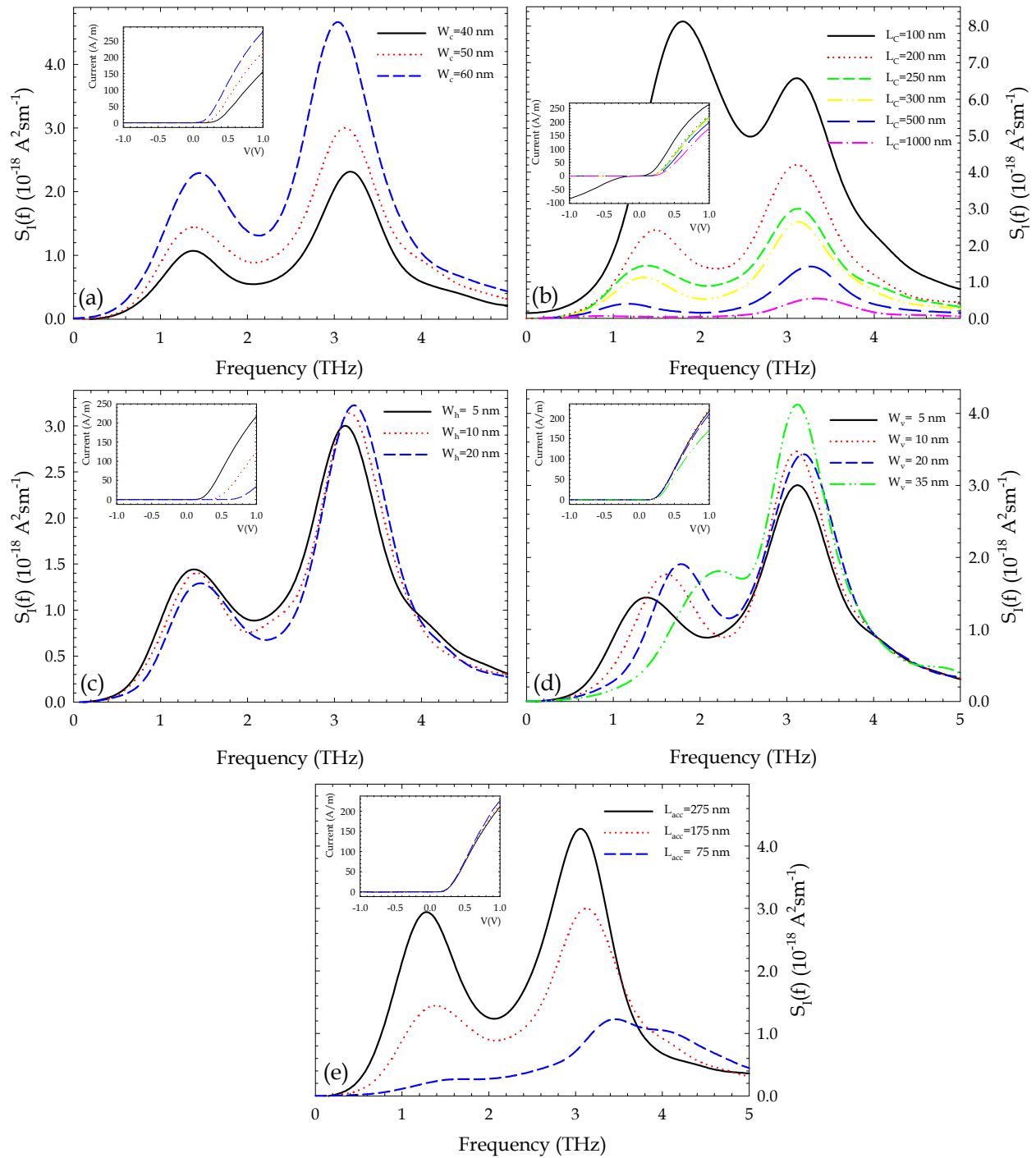


Fig. 16. Current-noise spectra at equilibrium when some parameters of the topology of the diode are modified: (a)  $W_C=40, 50$  and  $60$  nm, (b)  $L_C=100, 200, 250, 300, 500$  and  $1000$  nm, (c)  $W_h=5, 10$  and  $20$  nm, (d)  $W_v=5, 10, 20$  and  $50$  nm and (e) length of the accesses  $L_{acc}=275, 175$  and  $75$  nm. The insets show the corresponding I-V characteristics.

### 4.3 Rectification to AC signals

We have analyzed the dynamic behaviour of SSDs in terms of their AC to DC rectification (RF detection) as the main application of the device [Íñiguez-de-la-Torre et al., 2009b]. Harmonic voltage signals  $V=V_0\sin(2\pi ft)$  of increasing frequency  $f$  are applied between the contacts and the mean value of the output current is evaluated for the same “set” of SSDs than in the previous section [Fig. 17]. After a flat region at the lower frequencies, the rectified current exhibits a pronounced peak,  $f_p$ , just before the decay in the response. As expected,  $f_p$  depends on the channel length  $L_C$ , Fig. 17(a), being lower for longer channels. The SSD with  $L_C=100$  nm is correctly responding up to frequencies over 2.0 THz, thus making possible the operation of these devices as, for example, power detectors of THz waves. We also observe that  $f_p$  is highly sensitive to the properties of the vertical trench width  $W_v$  [Fig. 17(c)] but insensitive to that the horizontal trenches,  $W_h$  [Fig. 17(b)].

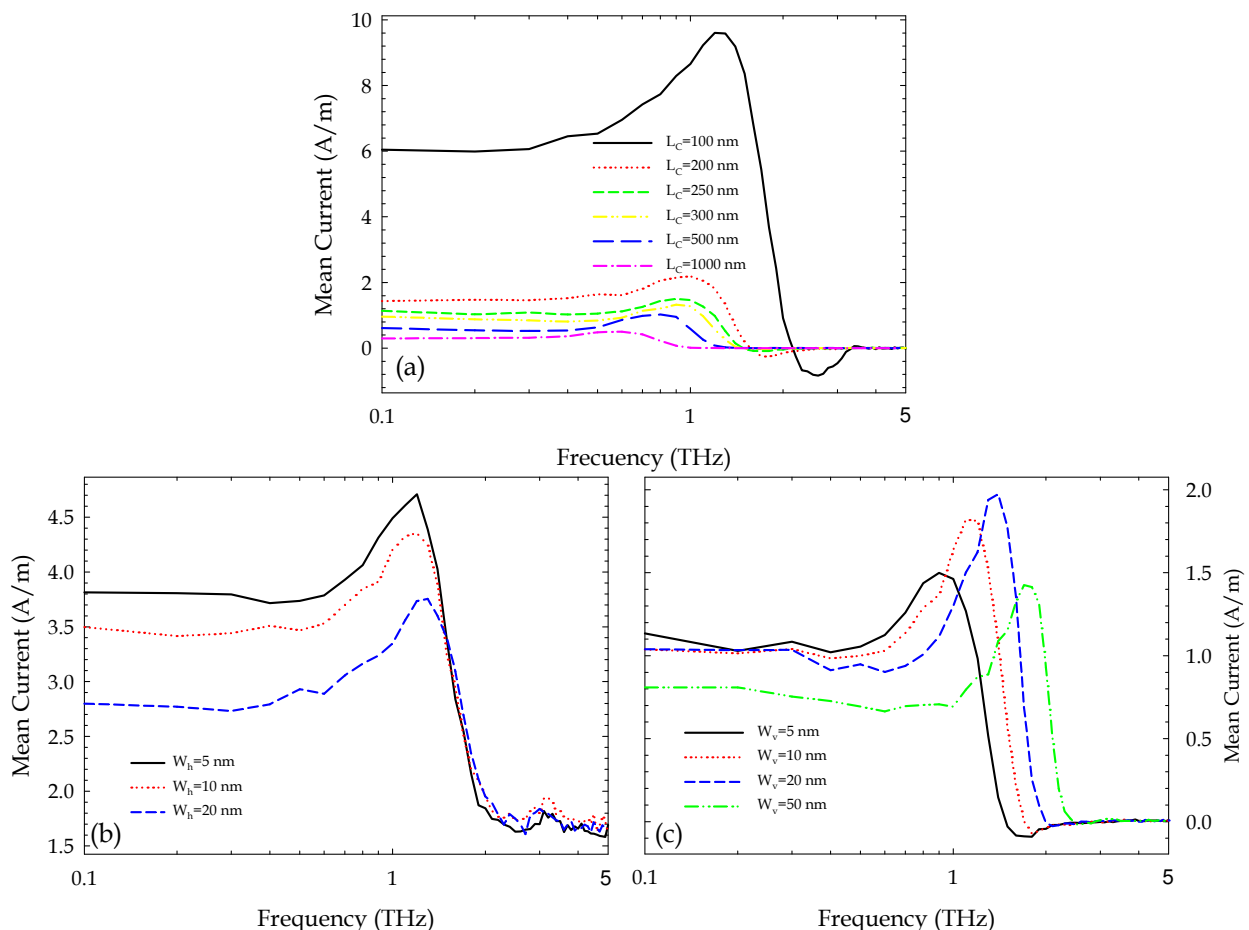


Fig. 17. Mean response current to a periodic input voltage (with amplitude of 0.25 V) applied to SSDs: (a)  $L_C=100, 200, 250, 300, 500$  and  $1000$  nm, (b)  $W_h=5, 10$  and  $20$  nm, (c)  $W_v=5, 10, 20$  and  $50$  nm.

Significantly, the behaviour of the low frequency peak in the noise spectra and its relative amplitude [Fig. 16] is in principle surprisingly similar to the  $f_p$  corresponding to the dynamic response of the rectified current [Fig. 17]. This indicates that we are observing the same microscopic phenomenon reflected in different macroscopic quantities. Let us explain this behaviour. The origin of the low frequency peak and  $f_p$  is related to the dynamics of the

reflected carriers (returning carriers) in the region close to both sidewalls of the vertical trenches, which capacitively couple to the current at the terminals. This coupling is modulated by two capacitors, one associated to the depletion regions at both sides of the trenches, and the other due to the vertical trenches themselves,  $C_v = \epsilon_v / W_v$  ( $\epsilon_v$  is the permittivity of the vertical trench). A more detail analysis of the effect of the insulator material filling the trenches can be found in [Íñiguez-de-la-Torre et al., 2009b]. That means that a typical noise mechanism, which is a collective charge fluctuation, is coupled due to the geometry provoking a resonant peak  $f_p$  in the AC to DC rectification. However the rectified current is phase shifted by the horizontal capacitor, while the noise is only influenced by the vertical one (with no need of the presence of a conducting channel), thus explaining why the frequency of the peak does not coincide exactly in both quantities. In addition the spectral density at equilibrium is proportional to the small signal admittance of the device, whereas the DC response current is caused by the diode rectification and corresponds to large signal conditions.

#### 4.4 InAs and InSb SSDs

The quite useful tuneable-by-geometry detection in the terahertz range observed in InGaAs SSD exhibit however a low amplitude and quality factor. In this section we will show how the low effective mass of InAs and InSb in relation to InGaAs enhances ballistic transport inside the diode, thus improving the detection sensitivity. A clear enhancement in the resonance and shifting  $f_p$  to higher frequencies is observed for these two narrow band gap materials [Fig. 18]. The resonance in the rectified DC current exhibits a remarkable quality factor, much higher than in InGaAs, with amplitude more than a hundred times the low frequency value in the case of InSb SSDs and also at higher frequency tuning range.

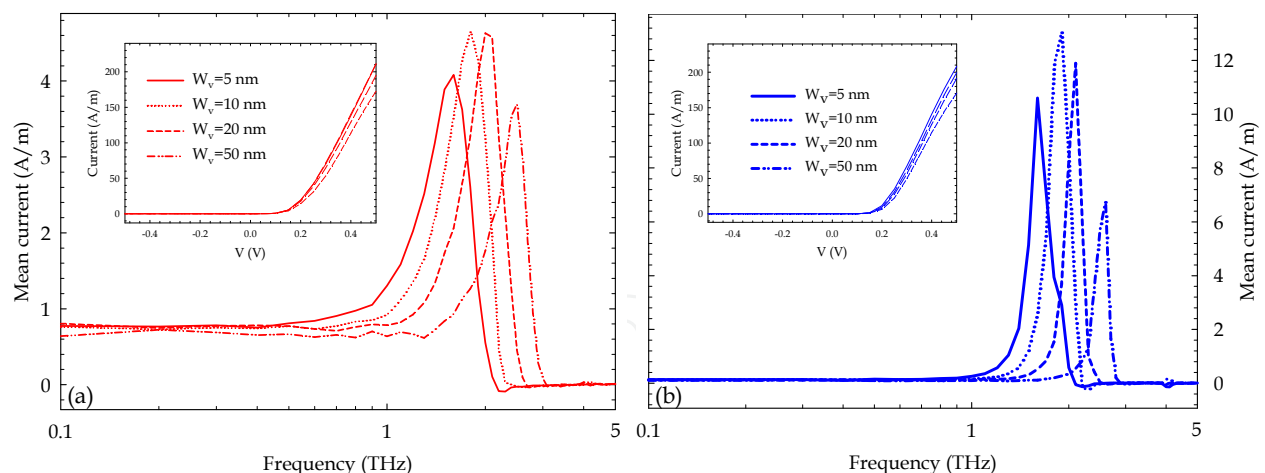


Fig. 18. Mean current response to a periodic input voltage (with amplitude of 0.15 V) applied to InAs-based SSD and (b) InSb-based SSD. The insets show the corresponding I-V curves.

To corroborate the clear link between the peak in the rectified DC current and the similar one present in the noise spectral density, in Fig. 19(a) we plot the noise spectra at equilibrium for SSDs based on three high mobility semiconductors: InGaAs, InAs and InSb (for  $W_v = 20$  nm). In Fig. 19(b), the frequency form noise peaks together with  $f_p$  of Fig. 17(c), 18(a) and 18(b) are plotted for each material. The three frequencies exhibit a similar relative

variation between the different materials, mainly affected by their effective masses and dielectric constants (0.014 and 17.65, respectively, for InSb, 0.023 and 15.15 for InAs and 0.042 and 13.88 for  $\text{In}_{0.47}\text{Ga}_{0.53}\text{As}$  [Rodilla et al., 2009]) thus revealing a common origin linked with plasma effects. Remarkably, the peak in the rectified DC current has the same tendency, certifying our previous conjecture that a noise mechanism is coupled via the particular geometry of the SSD to the DC to AC response and enhances the performance of the device.

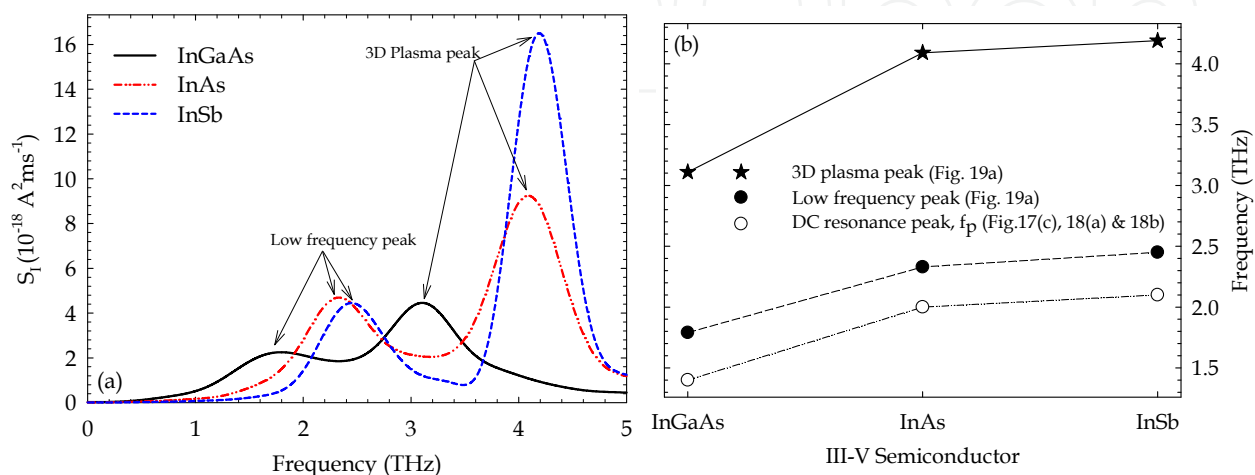


Fig. 19. (a) Current noise spectra at equilibrium for InGaAs, InAs and InSb diodes ( $W_V=20$  nm). (b) Comparison of the frequency peaks in the noise spectra with those of Fig. 17(c), 18(a) and 18(b).

## 5. Conclusion

Nowadays fabrication of narrow channels with a length of few nanometers is possible. Electrons move without suffering losses in their momentum and energy, leading to several new transport phenomena like ballistic transport. Our MC model treats the electrons in a billiard ball-like manner (classical), but it locally takes into account the effect of degeneracy by using the rejection technique (the scattering mechanisms are rejected when the final energy state is likely to be occupied). It is to be noted that as our study is focused on room temperature operation, quantum effects such as energy quantization can be initially neglected.

Monte Carlo simulations have significant advantages over other methods: there are no adjustable parameters (only material related microscopic parameters), it gives precise information about internal quantities (including scattering) and it is able to describe non-local non-static processes like ballistic transport and collective phenomena like plasma oscillations. In summary, it is able to provide static, dynamic and noise results with the only drawback of CPU intensive and slow simulations.

Monte Carlo simulations have shown that ballistic nanodevices like TBJs and SSDs have unique and striking high-frequency operation capability. However, there are significant problems to be solved. The reduction in length (so that the transport is almost purely ballistic) and width of the branches (enhancing the space charge effects), to optimize the performance of applications, greatly increases the impedance of the devices (to the range of k $\Omega$ ). As a consequence even very small parasitic capacitances (of the order of fF) prevent the



extrinsic cut-off frequencies of the devices to reach the THz range. Therefore, design guidelines for the reduction of the device parasitics, together with other ways of improvement as the use of more than one device in parallel must be used.

From a technological point of view the compatibility of these ballistic devices with the well-established high electron mobility transistors (HEMTs) circuitry should bring versatility for many practical applications, i.e. by allowing the processing of the signals generated by the ballistic devices. However, the final objective to potentially replace the conventional CMOS design flow and enable high performance analog and digital circuit design using this *family* of ballistic nanodevices, will require much more efforts directed towards the development of a logic compatible device, smaller interconnections, lower routing complexity, higher fabrication throughput, higher reliability, etc.

## 6. References

- Balocco C., Song A. M., Aberg M., Forchel A., González T., Mateos J., Maximov I., Missous M., Rezazadeh A. A., Saijets J., Samuelson L., Wallin D., Williams K., Worschech L. & Xu H. Q. (2005). Microwave detection at 110 GHz by nanowires with broken symmetry, *Nano Letters* 5, 1423.
- Balocco C., Halsall M., Vinh N. Q. & Song A. M., (2008). THz operation of asymmetric-nanochannel devices, *J. Phys.: Condens. Matter* 20, 384203.
- Bednarz L., Rashmi, Hackens B., Farhi G., Bayot V. & Huynen I. (2005). Broad-band frequency characterization of double Y-branch nanojunction operating as room-temperature RF to DC rectifier, *IEEE Trans. Nanotechnol.* 4, 576.
- Bednarz L., Rashmi, Simon P., Huynen I., González T. & Mateos J. (2006). Negative differential transconductance and nonreciprocal effects in Y-branch nanojunction. High-frequency behavior, *IEEE Trans. Nanotech.* 5, 750.
- Büttiker M. (1986). 4 terminal phase coherent conductance, *Phys. Rev. Lett.* 57, 1761 (1986).
- Cappy A., Bayot V., Bednarz L., Bollaert S., Boutry H., Gonzalez T., Hackens B., Huynen I., Gallo J. S., Mateos J., Pardo D., Rashmi, Roelens Y., Vasallo B. G. & Wallart X. (2005). Ballistic Nanodevices for Terahertz Data Processing, Nanotera EU IST-2001-32517 project 3rd year review report. Tech. Rep., Nanotera Consortium, February 2005, available online at: [http://www.phantomsnet.net/files/EUprojects/NANO\\_TERA\\_FR.pdf](http://www.phantomsnet.net/files/EUprojects/NANO_TERA_FR.pdf).
- Diduck Q., Irie H. & Margala M. (2009). A room temperature ballistic deflection transistor for high performance applications, *Int. J. of High Speed Electron. Syst.* 19, 23-31.
- Galloo J. S., Pichonat E., Roelens Y., Bollaert S., Wallart X., Cappy A., Mateos J. & González T. (2004). Transition from ballistic to ohmic transport in T-branch junctions at room temperature in GaInAs/AlInAs heterostructures, *Proc. of the 2004 International Conference on Indium Phosphide and Related Materials IPRM*, IEEE Catalog 04CH37589, 378.
- Gardès C., Roelens Y., Bollaert S., Galloo J. S., Wallart X., Curutchet A., Gaquiere C., Mateos J., González T., Vasallo B. G., Bednarz L. & Huynen I. (2008). Ballistic nanodevices for high frequency applications, *Int. J. Nanotechnology.* 5, 796.
- González T. & Pardo D. (1996). Physical models of ohmic contact for MC device simulation, *Solid-State Electron.* 39, 555.

- González T., Mateos J., Pardo D., Varani L. & Reggiani L. (1999). Injection statistics simulator for dynamic analysis of noise in mesoscopic devices, *Semicond. Sci. Technol.* 14, L37.
- González T., Vasallo B. G., Pardo D. & Mateos J. (2004). Room temperature nonlinear transport in ballistic nanodevices, *Semicond. Sci. Technol.* 19, S125.
- Hieke K. & Ulfward M. (2000). Nonlinear operation of the Y-branch switch: Ballistic switching mode at room temperature, *Phys. Rev. B* 62, 16727.
- Íñiguez-de-la-Torre I., Mateos J., González T., Pardo D., Galloo J. S., Bollaert S., Roelens Y. & Cappy A. (2007). Influence of the surface charge on the operation of ballistic T-branch junctions: a self-consistent model for Monte Carlo simulations, *Semicond. Sci. Technol.* 22, 663.
- Íñiguez-de-la-Torre I., Mateos J., Pardo D. & González T. (2008). Monte Carlo analysis of noise spectra in self-switching nanodiodes, *J. Appl. Phys.* 103, 024502, (2008)
- Íñiguez-de-la-Torre I., González T., Pardo D., Gardès C., Roelens Y., Bollaert S. & Mateos J. (2009a). Influence of the branches width on the nonlinear output characteristics of InAlAs/InGaAs-based three-terminal junctions, *J. Appl. Phys.* 105, 094504.
- Íñiguez-de-la-Torre I., Mateos J., Pardo D., Song A. M. & González T. (2009b). Noise and THz rectification linked by geometry in planar asymmetric nanodiodes, *Appl. Phys. Lett.* 94, 093512.
- Irie H., Diduck Q., Margala M., Sobolewski R. & M. J. Feldman (2008). Nonlinear characteristics of T-branch junctions: Transition from ballistic to diffusive regime, *Appl. Phys. Lett.* 93, 053502.
- Irie H. & Sobolewski R. (2010). Terahertz electrical response of nanoscale three-branch junctions, *J. Appl. Phys.* 107, 084315.
- Jacoboni C. & Lugli P. (1989). *The Monte Carlo method for semiconductor device simulation*, New York: Springer-Verlag.
- Kaushal V., Íñiguez-de-la-Torre I., Irie H., Guarino G., Donaldson W. R., Ampadu P., Sobolewski R. & Margala M. (2010). A study of geometry effects on the performance of ballistic deflection transistor, *IEEE Transactions on Nanotechnology*, in press, (published online DOI: 10.1109/TNANO.2010.2050069).
- Kim H., Min H. S., Tang T. W. & Park Y. J. (1991). An extended proof of the Ramo-Shockley theorem, *Solid-State Electron.* 34, 1251.
- Lai R., Mei X. B., Deal W.R., Yoshida W., Kim Y. M., Liu P.H., Lee J., Uyeda J., Radisic V., Lange M., Gaier T., Samoska L. & Fung A. (2007). Sub 50 nm InP HEMT Device with Fmax Greater than 1 THz, *IEDM Technical Digest*, 609.
- Landauer R. (1957). Spatial variation of currents and fields due to localized scatterers in metallic conduction, *IBM J. Res. Dev.* 1, 223.
- Lau B., Hartmann D., Worschech L. & and A. Forchel (2006). Cascaded Quantum Wires and Integrated Designs for Complex Logic Functions: Nanoelectronic Full Adder, *IEEE Trans. Electron Devices*, 53, 5, 1107.
- Lewén R., Maximov I., Shorubalko I., Samuelson L., Thylén L. & Xu H. Q. (2002). High frequency characterization of a GaInAs/InP electronic waveguide T-branch switch, *J. Appl. Phys.* 91, 2398.
- Mateos J., González T., Pardo D., Hoel V., Happy H. & Cappy A. (1999). Effect of the T-gate on the performance of recessed HEMT's. A MC analysis, *Semicond Sci. Technol.* 14, 864.

- Mateos J., González T., Pardo D., Hoel V., Happy H. & Cappy A. (2000a). Improved MC algorithm for the simulation of  $\delta$ -doped AlInAs/GaInAs HEMTs, *IEEE Trans. Electron Devices* 47, 250.
- Mateos J., González T., Pardo D., Hoel V., Happy H. & Cappy A. (2000b). MC simulator for the design optimization of low-noise HEMTs, *IEEE Trans. Electron Devices* 47, 1950.
- Mateos J., Vasallo B. G., Pardo D., González T., Galloo J. S., Roelens Y., Bollaert S. & Cappy A. (2003a). Ballistic nanodevices for terahertz data processing: Monte Carlo simulations, *Nanotechnology* 14, 117.
- Mateos J., Vasallo B. G., Pardo D., González T., Galloo J. S., Bollaert S., Roelens Y. & Cappy A. (2003b). Microscopic modelling of nonlinear transport in ballistic nanodevices, *IEEE Trans. Electron Devices* 50, 1897.
- Mateos J., Vasallo B. G., Pardo D., González T., Pichonat E., Galloo J. S., Bollaert S., Roelens Y. & Cappy A. (2004). Non-linear effects in T-branch junctions, *IEEE Elec. Dev. Lett.* 25, 235.
- Mateos J., Vasallo B. G., Pardo D. & González T. (2005). Operation and high-frequency performance of nanoscale unipolar rectifying diodes, *Appl. Phys. Lett.* 86, 212103.
- Müller C. R., Worschech L., Höpfner P., Höfling S. & Forchel A. (2007). Monolithically integrated logic NOR gate based on GaAs/AlGaAs three-terminal junctions, *IEEE Electron Device Lett.* 28, 859.
- Palm T. & Thylen L. (1992). Analysis of an electron-wave Y-branch switch, *Appl. Phys. Lett.* 60, 2, 237-239.
- Palm T. & Thylen L. (1996). Designing logic functions using an electron waveguide Y-branch switch, *J. Appl. Phys.* 79, 8076.
- Rahman S. F. B. A., Nakata D., Shiratori Y. & Kasai S. (2009). Boolean logic gates utilizing GaAs three-branch nanowire junctions controlled by Schottky wrap gates, *Jpn. J. Appl. Phys.* 48, 06FD01.
- Rashmi, Bednarz L., Hackens B., Farhi G., Bayot V. & Huynen I. (2005). Nonlinear electron transport properties of InAlAs/InGaAs based Y-branch junctions for microwave rectification at room temperature, *Solid State Commun.* 134, 217.
- Reitzenstein S., Worschech L., Hartmann P. & Forchel A. (2002). Logic AND/NAND gates based on three-terminal ballistic junctions, *Electronics Lett.* 38, 951.
- Reitzenstein S., Worschech L. & Forchel A. (2004). Room temperature operation of an in-plane half-adder based on ballistic Y-junctions, *IEEE Electron Device Lett.* 25, 462.
- Rodilla H., González T., Pardo D. & Mateos J. (2009). High-mobility heterostructures based on InAs and InSb: A Monte Carlo study, *J. Appl. Phys.* 105, 113705.
- Sadi T., Dessenne F. & Thobel J. (2009). Three-dimensional Monte Carlo study of three-terminal junctions based on InGaAs/InAlAs heterostructures, *J. Appl. Phys.* 105, 053707.
- Shorubalko I., Xu H. Q., Maximov I., Omling P., Samuelson L. & Seifert W. (2001). Nonlinear operation of GaInAs/InP-based three-terminal ballistic junctions, *Appl. Phys. Lett.* 79, 1384.
- Shorubalko I., Xu H. Q., Maximov I., Nilsson D., Omling P., Samuelson L. & Seifert W. (2002). A novel frequency-multiplication device based on three-terminal ballistic junction, *IEEE Elec. Dev. Lett.* 23, 377.
- Song A. M., Lorke A., Kriele A., Kothaus J. P., Wegscheider W. & Bichler M. (1998). Nonlinear electron transport in an asymmetric microjunction: a ballistic rectifier, *Phys. Rev. Lett.* 80, 3831.

- Song A. M. (1999). Formalism of nonlinear transport in mesoscopic conductors, *Phys. Rev. B* 59, 9806.
- Song A. M., Omling P., Samuelson L., Seifert W., Shorubalko I. & Zirath H. (2001). Operation of InGaAs/InP-based ballistic rectifiers at room temperature and frequencies up to 50 GHz, *Jpn. J. Appl. Phys.* 40, L909.
- Song A. M., Missous M., Omling P., Peaker A. R., Samuelson L. & Seifert W. (2003). Unidirectional electron flow in a nanometer-scale semiconductor channel: A self-switching device, *Appl. Phys. Lett.* 83, 1881.
- Song A. M. (2004). *Room temperature ballistic nanodevices*, Encyclopedia of Nanoscience and Nanotechnology, 9, 371-389.
- Sun J., Wallin D., Brusheim P., Maximov I., Wang Z. G. & Xu H. Q. (2007). Frequency mixing and phase detection functionalities of three-terminal ballistic junctions, *Nanotechnology* 18, 195.
- Sun J., Wallin D., Maximov I. & Xu H. Q. (2008). A novel SR latch device realized by integration of three-terminal ballistic junctions in InGaAs/InP, *IEEE Electron Device Lett.* 29, 540.
- Suyatin D. B., Sun J., Fuhrer A., Wallin D., Fröberg L. E., Karlsson L. S., Maximov I., Wallenberg L. R., Samuelson L. & Xu H. Q. (2008). Electrical Properties of Self-Assembled Branched InAs Nanowire Junctions, *Nano Letters* 8, 1100
- Vasallo B. G., González T., Pardo D. & Mateos J. (2004). Monte Carlo analysis of four-terminal ballistic rectifiers, *Nanotechnology* 15, S250.
- Wesström J. O., (1999). Self-gating effect in the electron Y-branch switch, *Phys. Rev. Lett.* 82, 2564.
- Worschech L., Xu H. Q., Forchel A. & Samuelson L. (2001a). Bias-voltage-induced asymmetry in nanoelectronic Y branches, *Appl. Phys. Lett.* 79, 3287.
- Worschech L., Fischer F., Forchel A., Kamp M. & Schweizer H. (2001b). High frequency operation of nanoelectronic Y-branch at room temperature, *Jpn. J. Appl. Phys.* 40, L867.
- Worschech L., Schliemann A., Reitzenstein S., Hartmann P. & Forchel A. (2002). Microwave rectification in ballistic nanojunctions at room temperature, *Microelectron. Eng.* 63, 217.
- Worschech L., Reitzenstein S., Hartmann P., Kaiser S., Kamp M. & Forchel A. (2003). Self-switching of branched multiterminal junctions: A ballistic half-adder, *Appl. Phys. Lett.* 83, 2462.
- Xu H. Q. (2001). Electrical properties of three-terminal ballistic junctions, *Appl. Phys. Lett.* 78, 2064.
- Xu H. Q. (2002). A novel electrical property of three-terminal ballistic junctions and its applications to nanoelectronics, *Physica E* 13, 942-945.
- Xu H. Q., Shorubalko I., Wallin D., Maximov I., Omling P., Samuelson L. & Seifert W. (2004). Novel nanoelectronic triodes and logic devices with TBJs, *IEEE Electron Device Lett.* 25, 164.



## **Applications of Monte Carlo Method in Science and Engineering**

Edited by Prof. Shaul Mordechai

ISBN 978-953-307-691-1

Hard cover, 950 pages

**Publisher** InTech

**Published online** 28, February, 2011

**Published in print edition** February, 2011

In this book, Applications of Monte Carlo Method in Science and Engineering, we further expose the broad range of applications of Monte Carlo simulation in the fields of Quantum Physics, Statistical Physics, Reliability, Medical Physics, Polycrystalline Materials, Ising Model, Chemistry, Agriculture, Food Processing, X-ray Imaging, Electron Dynamics in Doped Semiconductors, Metallurgy, Remote Sensing and much more diverse topics. The book chapters included in this volume clearly reflect the current scientific importance of Monte Carlo techniques in various fields of research.

### **How to reference**

In order to correctly reference this scholarly work, feel free to copy and paste the following:

Ignacio Iñiguez-de-la-Torre, Tomás González, Helena Rodilla, Beatriz G. Vasallo and Javier Mateos (2011). Monte Carlo Simulation of Room Temperature Ballistic Nanodevices, Applications of Monte Carlo Method in Science and Engineering, Prof. Shaul Mordechai (Ed.), ISBN: 978-953-307-691-1, InTech, Available from: <http://www.intechopen.com/books/applications-of-monte-carlo-method-in-science-and-engineering/monte-carlo-simulation-of-room-temperature-ballistic-nanodevices>

# **INTECH**

open science | open minds

### **InTech Europe**

University Campus STeP Ri  
Slavka Krautzeka 83/A  
51000 Rijeka, Croatia  
Phone: +385 (51) 770 447  
Fax: +385 (51) 686 166  
[www.intechopen.com](http://www.intechopen.com)

### **InTech China**

Unit 405, Office Block, Hotel Equatorial Shanghai  
No.65, Yan An Road (West), Shanghai, 200040, China  
中国上海市延安西路65号上海国际贵都大饭店办公楼405单元  
Phone: +86-21-62489820  
Fax: +86-21-62489821



© 2011 The Author(s). Licensee IntechOpen. This chapter is distributed under the terms of the [Creative Commons Attribution-NonCommercial-ShareAlike-3.0 License](#), which permits use, distribution and reproduction for non-commercial purposes, provided the original is properly cited and derivative works building on this content are distributed under the same license.

IntechOpen

IntechOpen